Six years of electrified convection over the island of Corsica monitored by SAETTA: General trends and anomalously electrified thunderstorms during African dust south flow events

Sylvain Coquillat, Véronique Pont, Dominique Lambert, Ronan Houel, Mickaël Pardé, Michaël Kreitz, Didier Ricard, Eric Gonneau, Pierre de Guibert, Serge Prieur

Version of Record: https://www.sciencedirect.com/science/article/pii/S0169809522002137
Manuscript_68134fe097c8b4425a1b35f10a575cb7

Six years of electrified convection over the island of Corsica monitored by SAETTA: general trends and anomalously electrified thunderstorms during African dust south flow events

Sylvain Coquillat[1], Véronique Pont[1], Dominique Lambert[1], Ronan Houel[1], Mickaël Pardé[2], Michaël Kreitz[2], Didier Ricard[3], Eric Gonneau[1], Pierre de Guibert[1], Serge Prieur[1]

[1]LAERO, Université de Toulouse, CNRS, IRD, UT3, Toulouse, France
[2]Ecole nationale de la météorologie, Météo-France, Toulouse, France
[3]CNRM, Météo France, CNRS, Toulouse, France

Correspondence to: Sylvain Coquillat (sylvain.coquillat@aero.obs-mip.fr)

Abstract. By means of the SAETTA 3D lightning mapping array, the total lightning activity has been detected in a 240 km × 240 km square domain centred on the island of Corsica located in the West Mediterranean basin, and characterized by a maritime and mountainous environment, with a complex and relatively high relief. The study period covers the months from April to December of the 6 years from 2014 to 2019. Observations are reported with a horizontal resolution of 1 km and a vertical resolution of 0.1 km in terms of density of VHF sources emitted by lightning, and of number of lightning day, in plane- and vertical- projections. Vertical distributions of VHF sources are also provided monthly for the whole period and over the full domain. These 3D long term observations show that the number of lightning days is more important on the main relief of the island. The density of VHF sources exhibits a sharp maximum over the confluence area of the 3 main valleys in the center of the northern part of the island, characterized by a recurrent and vertically well developed lightning activity. The period from 11:00 UTC to 14:00 UTC in July, and in a lesser extent in June and August, is at the origin of this density maximum. This behavior is thus due to a diurnal convection. The whole lightning activity is characterized by 2 maxima in June and September. The first one is linked with the diurnal convection in phase with the maximum elevation of the Sun. The second one must be due to usual large-scale organized thunderstorm events of the fall season. The vertical distribution of VHF sources exhibits an increase in the number of VHF sources from April to August at all altitudes, as well as an increase in the altitude of the main upper peak (from 5.8 km to 10 km) and of the secondary lower peak (from 4.2 km to 6.7 km) of this distribution. From August to December, the opposite evolution appears, except that October is characterized by a strong anomaly with a single intense lower peak at 5.5 km, apparently due to 2 strong events corresponding to anomalously electrified thunderstorms. Several of these anomalously electrified thunderstorms (negative dipoles) are reported. They are all characterized by the movement of cloud cells spatially small and relatively undeveloped vertically propagating from southwest to northeast and associated with a strong transport of desert dust from the African continent. The analysis of the meteorological environment of some of the studied events allows concluding that in each of the studied cases elevated convection was triggered, above the relatively dry atmospheric boundary layer characterized by a strong convective

inhibition. The low cloud liquid water content which is a key parameter of the non-inductive charging process is probably a good candidate to explain the anomalous electrification of these events.

1 Introduction

1.1 3D lightning observation

For meteorology, lightning is a signature for intense convective systems and provides interesting information on cloud physics since lightning is at the end of the chain of physical processes involved in thunderstorms. Lightning observations can then be used to characterize convection with an electric point of view. The most efficient solution to observe lightning in 3D at high temporal and spatial resolutions - only at regional scale - is based on the use of a Lightning Mapping Array (LMA) allowing detection of the radiation sources in the Very High Frequency (VHF) range (here after VHF sources) emitted by the propagating discharges (Thomas et al., 2004).

Few previous studies have reported regional 3D lightning climatologies accomplished using on 3D imager data. Fuchs et al. (2016) performed a first climatology based on VHF sources detected by 3 LMAs in the United States (Washington DC over 8 years, northern Alabama over 7 years, Northeast Colorado over 3 years) and also based on lightning deduced from a clustering method. They focused on different characteristics of lightning (2D maps of annual densities and duration, radial vertical profile of the initialization altitude...) for the total period without exploring daily, monthly, interannual variabilities. More recently Coquillat et al (2019) showed a first 2D analysis of the behavior of electrical activity in Corsica over 3 years in terms of density of VHF sources and days of electrical activity on various time scales (total period, day/night, June to September, interannual). The present study takes advantage of the 3D lightning imager SAETTA deployed in Corsica since summer 2014 (Coquillat et al., 2019) to further explore the characteristics of intense convection on this island. To our knowledge, this is the first time that long-term 3D observations are devoted to the analysis of electrical activity on interannual, monthly and hourly scales, using such a lightning imager.

1.2 Long-range lightning detection regional climatology

On the other hand, several lightning climatologies have been carried out over Europe in recent years by means of long-range lightning detection network operating in the very low frequency. Soriano et al (2005) analyzed the 10-year annual and diurnal cycles of the number of Cloud-to-Ground (CG) lightning observed in the Iberian Peninsula by the lightning detection network of the Instituto Nacional de Meteorologia in Spain. Anderson and Klugmann (2014) and Enno et al. (2020) have reported long-term observations made using the Arrival Time Differing NETwork (ATDnet). They showed 5-year lightning densities at annual and monthly scales while Enno et al. (2020) extended the observation period over a decade and showed a decadal climatology over Europe in terms of 2D lightning density and thunderstorm days, as well as in terms of months of the year with higher activity with also a study of seasonal variability. Kotroni and Lagouvardos (2016) performed a 10-year analysis of electrical activity over the Mediterranean, observed by ZEUS, and based on the number of days of thunderstorms

over the total period and on the lightning stroke density at seasonal scale. Galanaki et al. (2018) provided additional results to this study of Kotroni and Lagouvardos (2016) in terms of number of thunderstorm days. Poelman et al (2016) performed a 9-year climatology of CG lightning over Europe using the European Cooperation for Lightning Detection (EUCLID) network. They produced 2D maps of lightning density over the total period on a monthly scale. Taszarek et al. (2019) have more recently completed a pan-European thunderstorm day climatology based in part on 10 years of CG lightning observations from the EUCLID and ZEUS networks. They have produced 2D maps of the number of days with thunderstorms over the whole period and on a monthly scale, with a focus on the periods of highest activity.

1.3 Convection in the Corsican region

At regional scale, the influence of islands on the triggering of thunderstorms is of particular interest (e.g. Wilson et al., 2001; Qian, 2007, Lagouvardos et al., 2020). Mountainous islands turned out to be most effective in this process, because sea breezes and valley winds that are roughly in phase with each other may combine to strengthen the diurnal cycle of winds and form convergence zones during daytime (Kottmeier et al., 2000, Barthlott and Kirshbaum, 2013). Corsica is relatively large (8740 square kilometers) and is the highest island in the western Mediterranean basin. Its highest elevation reaches 2710 m, with about 20 mountains being higher than 2000 m (see the relief in Appendix A1). For instance, among the 735 world islands culminating at more than 400 meters of altitude and referenced by the UN, only 34 have higher summits (http://islands.uneop.ch/). The main mountain range runs roughly from northwest to southeast and the island's horizontal extent is about 80 km (W-E) ×180 km (S-N). Corsica is regularly affected by intense meteorological events such as heavy precipitation, wind storms and lightning (Lambert et al., 2011).

Thunderstorms are common on the mountainous coastal regions boarding the Mediterranean. Scheffknecht et al. (2017) presented a climatology of heavy precipitation over Corsica in the period 1985–2015. This climatology based on 173 events shows that the eastern half of Corsica, specifically over the relief, is most affected by high precipitation events. The months from September to December, most of all October, are identified as most prone to heavy precipitation events over Corsica. Using a climatological approach for a 5-y period, Ricard et al (2012) have shown that lightning activity is present in almost all heavy precipitation cases considered during autumn over southern France, including Corsica, indicating that deep moist convection is usually involved to produce high rainfall rates. Composite maps of lightning impacts occurring all along these Heavy Precipitation Events (HPEs) also show that the east of Corsica is one of the areas most exposed to a great number of impacts. The convective activity is then sustained by a moist southerly low-level jet along the eastern coast of Corsica. During the first Special Observation Period (SOP1) of the Hydrological cycle in the Mediterranean EXperiment (HyMeX) project (Ducrocq et al., 2014), the impact of the island of Corsica in terms of orographic, thermal, diabatic, and aerodynamic influence has been investigated on the initiation and evolution of diurnal convection, mesoscale convective systems, and on the embedded convection in cyclones.

Metzger et al. (2014) investigated the influence of upstream flow on the initiation of moist convection over Corsica using semi-idealized simulations. It is found that deep convection can only develop with high solar radiation and the wind direction can be the determining factor for the initiation of deep convection and also controls the location of precipitation. It is further found that the impact of saturation deficit is higher than the impact of stability. With increased instability, the atmospheric conditions are more favorable for the development of convection however the high saturation deficit in the middle troposphere prevents the formation of deep convection. The variability of water vapour and pre-convective conditions over the mountainous island of Corsica are presented by Adler et al. (2015). They show that spatial inhomogeneities in the pre-convective atmospheric conditions evolved and the knowledge of these turned out to be crucial to understand the timing and location of isolated deep convection over the island.

1.4 About the aerosol influence

According to Williams et al (2004) the flash activity on an island should be related to its area (surface). Smaller islands have a low lightning activity typical of a marine environment and thus a low land-sea contrast, whereas larger islands have an intense lightning activity with a high land-sea contrast. The transition between the two behaviors appears to be around 100 to 1000 square kilometers. Their analysis of the land-sea contrast was based on the thermal hypothesis on the one hand and the aerosol hypothesis on the other. According to the thermal hypothesis, the earth's surface becomes warmer than the sea surface under the influence of solar radiation, which destabilizes the atmosphere above the earth more easily and causes the development of strong updrafts that reinforce the formation of ice crystals at high altitudes, thus strengthening the electrification process. According to the aerosol hypothesis, an enhanced number of cloud condensation nuclei leads to an enhanced number of small cloud droplets, which weakens the warm rain coalescence process and enables more cloud water to reach the mixed phase region and participate in the electrification process. While they considered that the aerosol hypothesis could explain the greater lightning activity over large islands as it is the case with the convection on a continental scale, they concluded that the dependence of lightning activity vs. island area is more consistent with the thermal hypothesis. It is worth noting that aerosols themselves have also a radiative impact. Flamant et al., 2015 numerically studied the radiative impact of desert dust on orographic rain in the Mediterranean basin. In their study, while the dust radiative impact is well captured, it only marginally affects the rainfall amounts and location.

1.5 Thunderstorm electrification

The primary source of thunderstorm electrification appears to be the non inductive charging mechanism (in the absence of a pre-existing electric field) involving rebounding collisions between small ice particles and rimed graupel in the presence of supercooled liquid water (see Saunders, 2008). If the cloud liquid water content (LWC) ranges from about 1 to about 3 g m^{-3}, the collisions bring positive charge to ice crystals and negative charge to graupel for altitudes higher than the -10 °C isotherm, and opposite charge for altitudes lower than this -10°C isotherm. Due to the sedimentation of the larger particles (graupel) and the transport of the smaller in the updraft (ice crystals), the electric charges separate so that positively charged

ice crystals are found at high altitude, negatively charged graupel and negatively charged crystals at mid level, and positively charged graupel at low level in the cloud. The thunderstorm cloud is then theoretically constituted of three superimposed layers of charges (positive/negative/positive), which corresponds to most observations in temperate latitude thunderstorms. Laboratory studies (e.g., Emersic and Saunders, 2010; Jayaratne et al., 1983) have also found that the presence of unusually high or low cloud LWC causes graupel to acquire a positive charge and ice crystals to acquire a negative charge during the collisions, regardless of the temperature/altitude in the mixed phase region. In this case, negative ice crystals are transported aloft meanwhile positive graupel sediment, resulting in the presence of a negative charge layer at high altitude with a positive charge at mid level in the thunderstorm cloud.

1.6 Electrical structure of storms

In terms of electrical structure, thunderstorms can exhibit various electrical charge distributions, each corresponding to a particular denomination of electrical structure. Figure 1 illustrates the usual vertical charge structures in updraft cores reported so far (see Stolzenburg et al., 1998; Bruning et al., 2014; Fuchs et al., 2015). The usual normal tripole structure (Figure 1a) is dominated by a negative charge layer at mid level of the thundercloud depth with a positive charge layer above, and a secondary positive charge layer at the lowest level (Williams et al., 1989). This structure therefore consists of an upper positive dipole and a lower negative dipole. The upper positive charge layer of the normal tripole structure is most often considered more electrically active than the lower positive charge layer (Lang and Rutledge, 2011). This bulk distribution of charge is likely to be observed in the updraft cores and it can be much more complex in the downdrafts with more numerous charge layers (see Bruning et al., 2014). Complex charge structures have also been observed in supercells or mesoscale convective system (Stolzenburg et al., 1998; MacGorman et al., 2005).

Anomalous charge structures corresponding to Figure 1b and 1c have also been observed in US great plains (Lang et al., 2004; Rust et al., 2005; Tessendorf et al., 2007; MacGorman et al., 2008) and recently in the Southeastern United States (Stough and Carey, 2020; Stough et al., 2021). The inverted tripole storms had a midlevel positive charge layer where a negative one is expected in regular storms. These anomalous charge structures tend to produce severe weather (Lang and Rutledge, 2011) and to be responsible of the production of storms with predominantly positive CG flashes (Tessendorf et al. 2005; Lang et al., 2004, Wiens et al., 2005). Nevertheless, some of these anomalous storms have also produced little flash rate and no positive CG dominance. Bruning et al. (2014) suggested that the term “inverted” could be misleading since a storm can have a more complicated or different vertical charge structure than the normal and inverted ones. In recent studies, the term “anomalous” is used to classify storms or parts of storms which are not identified as classical tripolar charge structure (Figure 1b, 1c, 1d). Since normal polarity storms have a dominant positive upper charge regions around -40°C, Fuchs et al. (2015) have described anomalous storms as storms with a dominant positive layer at temperatures warmer than -30°C. Thus, this classification of anomalous storms concerns storms with strong midlevel positive charge layer and storms with a dominant lower positive layer.

Williams et al. (2005) considered that an elevated cloud base height may result in a large cloud liquid water content in the mixed phase region. They also considered that large quantities of Cloud Condencsation Nuclei (CCN) in the boundary layer could lead to shift of the droplet size spectrum towards small dimensions resulting in a suppression of coalescence and hence here again in a large cloud liquid water content in the mixed phase region. Both processes would lead to the positive charging of graupel and hence to an anomalous charge structure of the cloud. Carey and Buffalo (2007) showed that anomalous electrical structures of severe thunderstorms were notably characterized by an environment associated with, among other things, a dry lower troposphere, a higher cloud base height, a smaller warm cloud depth, and more intense unstable conditions. The lack of aerosol data prevented them from analyzing the possible role of CCNs on thunderstorm electrification. Other authors have discussed the role of environmental conditions on the anomalous electrification of thunderstorms (Lang & Rutledge 2011; Chmielewski et al. 2018; Fuchs et al. 2018). Stough et al. (2021) have addressed comparisons between anomalous and normal supercells within a same region, i.e. the Southeastern United States. By considering regional variability between charge structures and environmental conditions in intense deep convection, they evaluated hypotheses concerning the kinematic, microphysical and environmental support for anomalous charge structures. Other anomalous charge structures have been observed outside USA, for instance: negative dipole and inverted tripole in Japanese winter storms (Zheng et al., 2019), a multicell storm in the Qinghai-Tibet plateau showed at some point negative dipole structure (Li et al., 2017), bi-level negative flashes in a tropical thunderstorm in Columbia (Lopez et al., 2019) and anomalous storms with low altitude lightning in Argentina during the RELAMPAGO field campaign (Lang et al., 2020).

Furthermore, the distribution of charge in the tripole structure can vary in an important way leading to top-heavy or bottom-heavy tripole structures (Figure 1c) depending on the relative strength of positive charge layers (e.g. Mansell et al., 2010). For instance, Qie et al. (2005) and Bruning et al. (2007) observed thunderstorms respectively over Tibetan Plateau (China) and Oklahoma (USA) with a low flash rate (1flash/min or less on average) that appeared to begin with lightning in the lower negative dipole, and the subsequent lightning activity occurred mainly in the lower part of the storm. These observations appear thus consistent with the "bottom-heavy" qualification of Mansell et al. (2010).

Sometimes the upper positive charge layer of the normal tripole structure (Figre 1a) may be absent and the charge structure of the cloud is then reduced to what is called a lower negative dipole (Figure 1d), with a negative charge layer at mid level above and a positive charge layer below. This type of electrical structure was observed by Salvador et al. (2021) in Catalonia, northeast of the Iberian Peninsula. They also reported charge structures under the form of an upper positive dipole (i.e. a positive charge layer at high altitude above a negative charge layer at mid level).

The methodology followed in the present study is described in Section 2; the general characteristics of the convection over the global period are presented in Section 3 and declined on inter-annual, monthly, and hourly bases. The next part (Section 4) is devoted to particular observations of anomalously electrified storms characterized by a negative dipole structure with a focus on the environmental conditions that prevail in the case of these atypical events, which are then discussed (Section 5).

2 Methodology

2.1 SAETTA data and processing

SAETTA is a 3D lightning imager based on 12 LMA stations (designed by New Mexico Tech, USA) deployed in Corsica since summer 2014. Its overall characteristics and performances are described by Coquillat et al. (2019). Basically, the electromagnetic radiation emitted by propagating discharges is detected in the form of pulses in a specific range of the VHF domain (60-66 MHz) at time intervals of 80 µs. The use of at least 6 detection stations and the time-of-arrival method (Thomas et al., 2004) allows to determine with high spatial and temporal accuracies the position and the date of the lightning element that emitted the detected pulse in a given time interval (called VHF source in the following). The maximum detection range is about 350 km from the center of Corsica. However, for reasons of location accuracy that degrades with distance (Koshak et al., 2004; Thomas et al., 2004, Coquillat et al., 2019), of source and flash detection efficiency (Boccippio et al., 2001; Thomas et al., 2001; Fuchs et al., 2016; Chmielewski and Bruning 2016), and of difficulty in detecting VHF sources in the lower layers due of the rotundity of the Earth, the study area is limited to a square of 240 km side centered on Corsica.

The study period covers the months of April to December from 2014 to 2019, but a few months are missing in the early years because the network was initially operational from 13/07/2014 to 20/10/2014, then from 11/04/2015 to 01/12/2015, and continuously after 13/04/2016 (see overview of available data in Appendix A2). Fortunately, the months that are missing are not the most active months or months of interest except for June and November 2014. From then on, when a month is mentioned it implies that the results concerning this month are de facto based on the availability periods only. The VHF sources data and their quicklooks are available on the following web link: https://saetta.aeris-data.fr/. As in Coquillat et al. (2019), present study considers only VHF sources that have been determined with a minimum of 7 stations and with a goodness of fit value $\chi_v^2 \leq 0.5$ (for details see the conclusion and Section A2 of Thomas et al., 2004). Both values were empirically determined at the flash scale to disregard all isolated points without altering the flash structure.

The 3D long term observations (LTO) are built on a 3D mesh domain with a resolution of 1 km × 1 km in the horizontal plane of the 240 km × 240 km square, and a resolution of 0.1 km in the vertical direction between 0 and 15 km altitude. It first concerns the number of VHF sources in each 1 km × 1 km pixel, which gives a good indication of the intensity of electrical activity. The same procedure is used in the vertical W-E and S-N projections in each 0.1 km × 1 km pixel. The vertical profile of the number of VHF sources integrated on the whole domain is also computed and displayed under the form of an altitude histogram of VHF sources from 0 to 15 km altitude with 0.1 km depth bins. LTO then concern the number of days of lightning. The number of days of lightning in a given 1 km × 1 km pixel is defined as the total number of days during which at least 5 VHF sources have been detected, i.e. number of so called lightning days hereafter. This corresponds to 5 sources in a volume of 1 km × 1 km × 15 km, i.e. 5 sources in a voxel of 15 km^3. The value of 5 sources was determined empirically to ignore isolated sources corresponding to residual noise or poorly located sources, while

retaining low lightning activity events (Coquillat et al., 2019). In the vertical projection, this threshold of 5 sources is no longer appropriate because the pixels have a vertical area of only 0.1 km x 1 km and a horizontal length of 240 km, i.e. they are voxels of volume equal to 24 km^3. Keeping the same ratio of number of VHF sources to voxel volume so that the results are homogeneous, the threshold of VHF sources for a lightning day was therefore set at 8 VHF sources per pixel in each W-E and S-N vertical plane.

According to Chmielewski and Bruning (2016), who developed a performance evaluation tool for LMA networks in the United States, source and lightning detection efficiencies remain relatively high (about 95%) within the nearest 100 km from the center of these LMA networks. Performance logically decreases at longer ranges, with a dependence on the station configuration and thresholds. In the present study, where the domain is a 240 km square (i.e., containing a 120 km radius circle), we will see in Section 3.1 that most of the electrical activity detected by the SAETTA network is essentially distributed within the first 100 km (cf. Figure 2c), so the potential decrease in detection efficiency with distance should not substantially affect the observations reported in the present study.

LTO are also considered on inter-annual, monthly and hourly bases. For the inter-annual and monthly bases, the number of VHF sources is determined over the entire 240 km × 240 km domain while the number of lightning days corresponds to the dates when at least one pixel is affected by a lightning event (i.e. the pixel contains 5 VHF sources in the horizontal plan or 8 VHF sources in the vertical plan). One must keep in mind that if a day passes without any thunderstorm event on the domain but a piece of lightning from a thunderstorm outside the domain is present even on a single pixel, then that date will be considered a lightning day. For the hourly basis, the number of lightning days per pixel - only on the horizontal projection - was determined for each one-hour period in UT time. This corresponds to the 2014 to 2019 cumulative number of lightning days per pixel for each one-hour period.

One of the main advantages of lightning observation by the LMA network is to obtain a 3D mapping of the VHF sources corresponding to the lightning branch elements. It is also possible to have access to the polarity of the charge layers in which the discharges propagate. Indeed, the LMA system provides information on the power with which each VHF source is detected. Now, the propagation of a positive leader through a negative charge region does not emit radiation as strongly in the VHF portion of the electromagnetic spectrum as the propagation of a negative leader through a positive charge region, and so there are fewer detections in the negative charge region (e.g., Shao and Krehbiel 1996; Rison et al., 1999; Maggio et al., 2005; Rust et al., 2005). As a matter of fact, the power of the electromagnetic radiation produced by a discharge is proportional to the time variation of its electric current. However, negative discharges - which propagate in the positive charge layer - are intermittent and erratic discharges for which the electric current is highly variable and thus that radiate with relatively high power, while positive discharges - which propagate in the negative charge layer - are more continuous discharges with lower radiation. The intensity of the radiation received is thus an indicator of the polarity of the discharges (Thomas et al., 2001) and therefore of the polarity of the cloud zones, which makes it possible to identify the electrical

structure of a storm cell (normal tripole, anomalous charge structures like inverted tripole, bottom heavy tripole, negative dipole, etc.).

To determine the polarity of the charge layers in which a flash propagates, we first look at its spatial and temporal development (XLMA software, Thomas et al., 2003). According to the physical model of lightning discharge (Kasemir, 1960), the flash develops bidirectionally from a trigger point in the form of a negative leader propagating towards the positive layer of the cloud and a positive leader propagating towards the negative layer of the cloud. As specified by Wiens et al. (2005), the initial VHF sources of the flash are assumed to correspond to the negative discharge. Since this negative discharge emits more powerful electromagnetic radiation, it is more easily detected by the LMA and therefore more documented than the positive discharge. The positive layer can thus be identified from the numerous VHF sources of the negative discharge after its initialization phase. The negative layer corresponds to the VHF sources of the positive discharge whose weaker electromagnetic radiation leads to a much lower density of VHF sources. However, the diagnosis of the power with which each source is detected is essential for the analysis to be totally reliable. It avoids misinterpretation as in the example of Figure 10 where a normal tripole characterized by an upper positive dipole with low activity (Figure 10 bottom) could be erroneously considered as a negative dipole (Figure 10 top) since both have the same vertical profile of the number of sources (frames c).

2.2 Meteorological data

The study of the meteorological situations is made through the Earth visualization tool (https://earth.nullschool.net/) allowing access to the Global Forecast System (GFS, 0.25° horizontal resolution, https://www.emc.ncep.noaa.gov/users/meg/gfsv16/) datasets delivered by the NOAA/NWS Environmental Modeling Center. The geographical area of the western Mediterranean basin is considered, taking into account the island of Corsica. In order to know the large-scale atmospheric flow sweeping the island of Corsica and its reliefs, it is possible to extract for a given grid cell the wind modulus and direction for different levels of the model. The best compromise is to study these parameters at the 850 hPa level in order to consider a large-scale atmospheric flow not disturbed by relief flow effects but potentially influencing the atmospheric content and convective dynamics near the reliefs. Tests have been carried out between island and maritime areas at different levels of the model to converge towards this compromise. For a given storm event the wind speed and wind direction at 850 hPa are considered at the center of Corsica Island at the time before and during the event. As GFS does not resolve meso-scale convective system, we can consider the wind data are representative of the large scale flow.

Furthermore, a synoptic situation analysis is made for each of specific June 2019 events (see section 4.4). The synoptic context is studied for the mid-altitude layer (ZT500 field, corresponding to the 500 decameter geopotential – damgp - height, about half the tropopause height), for the surface layer (Mean Surface Level Pressure (MSLP) and wet bulb potential temperature θ'_w), and for the Potential Vorticity1.5 layer (PV height in decameter geopotential and wind speed). These layer

characteristics were extracted from Météo-France (the French national weather service) archive corresponding to predictions and analysis performed operationally by ARPEGE, the French hydrostatic Numerical Weather Prediction (NWP) model. This study allows us to infer: (i) the convective situation - cold or warm air advection for mid altitude and surface layers, (ii) the participation of tropospheric anomaly to the convection, and (iii) the layer global Lagrangian trajectory - wind direction. Once the synoptic situation analyzed, we use the Applications of Research to Operations at MEsoscale (AROME) non-hydrostatic high resolution French NWP model (Seity et al., 2011) to identify the origin of the convection by analyzing vertical profiles representation of the complete temperature profile.

2.3 Aerosol data

The life cycles of clouds are controlled by an intimate interplay between meteorology and aerosol-and-cloud microphysics, including complex feedback processes (Myhre et al, 2013, Chen et al., 2021). To complete this long-term lightning study, we aim to provide information on the aerosol content of the atmosphere in order to possibly identify a trend on specific events. To do so, we use the Goddard Earth Observing System data (GEOS-5) from the Global Modeling and Assimilation Office (GMAO, Rienecker et al., 2008), and those from the Copernicus Atmosphere Monitoring System (CAMS– ECMWF, https://confluence.ecmwf.int/display/CKB/CAMS%3A+Reanalysis+data+documentation) visualized and extracted through the Earth tool (https://earth.nullschool.net/), at the point of latitude 42.42° N and of longitude 9.19° E, on Corsica. We thus have access to modeled data of Atmospheric Optical Thickness for Dust at 550 nm (AOT Dust). The more intense this parameter is, the more dust is concentrated in the atmospheric column, which can attenuate the incoming intensity of the considered wavelength. To evaluate these modeled data and to ensure the content of the Corsican atmosphere in coarse aerosol, we also use the AErosol RObotic NETwork (AERONET) data (https://aeronet.gsfc.nasa.gov/; Dubovik et al., 2006) from the Ersa measurement site (Cap Corse - 43.00367° N, 9.35929° E), when available. This remote site is isolated from any major anthropogenic source of aerosols and the total AOT data can be considered as representative of an atmospheric background, and of a long range transport of aerosols contained in the atmospheric column. Level 1 and level 2 AOT data at 500 nm as well as the Spectral Deconvolution Algorithm (SDA) fine mode fraction retrieved parameter (contribution of the fine mode of the aerosol population to the 500 nm AOT value) are used when available. When AOT Dust (dust aerosols only) is not available in the GEOS5 and CAMS databases (mainly in 2014 and 2015), we consider the total AOT from the AERONET database at Ersa site. The total AOT stands for the extinction along the atmospheric column due to all types of atmospheric aerosols. The SDA fine mode fraction is used to establish the size of the sphere in the figures as a proxy of the aerosol size contributing mainly to the AOT Dust or to the total AOT.

3. Lightning event observations over the 2014-2019 period

3.1 Total VHF sources density and lightning day distributions

The overall observations performed with the SAETTA network are firstly presented in terms of VHF source density and lightning day frequency. Figure 2 left represents the density of VHF sources per square kilometer according to different projections (horizontal, vertical cumulated on the latitude, vertical cumulated on the longitude). This materializes all the VHF sources observed from 2014 to 2019 by SAETTA. In this Figure 2c, one can observe a high density of sources in the center of Corsica which corresponds to strong vertical developments centered on a geographical area at the crossroads of three large valleys (approximate coordinates on the map in Appendix A1: +10 km West-East and +12 km South-North). However, this representation has little statistical representativeness because it may be conditioned by the single occurrence of an intense event. Thus, Figure 2g gives the number of days where the detection of sources is higher than 5 sources per day per square kilometer. This threshold of 5 excludes days with too few sources in a pixel, i.e., sources that do not correspond to flash but to noise (Coquillat et al. 2019). Strong frequencies of lightning days, characterized by red color density in Figure 2 right, are located over the main central relief, and also and especially over the North-East center mountainous region called Castagniccia (approximate coordinates on the map in Appendix A1: +20 km West-East and 0 km South-North). The maximum of VHF sources observed there (Figure 2 left) corresponds thus to a high frequency of days in which storms occurred. This reveals a place where there are often very active thunderstorms electrically with strong vertical development, associated with strong and intense convection. We can also see in the northeast corner of the domain a trail corresponding to non-negligible frequencies of occurrence (yellow/green colors) associated with a displacement/spreading of thunderstorm cells to the leeward in the northeast, the wind often coming from the southwest. Another extension of secondary lightning activity appears offshore near the southeast coast; it is favored by base-layer convergence processes by southeast flow (e.g. Barthlott et al., 2016).

3.2 Monthly variability of lightning day distribution

If we are now interested in the monthly variability of the SAETTA cumulative observation over the period 2014-2019, the densities of VHF sources and the frequencies of lightning days are represented for each month (see Figures 3, 4, 5) to give a statistical weight on the recurrence of events. In April (Figure 3 left), the observations made show little electrical activity. The electrical activity occurs on the relief, with a maximum of 6 lightning days per square kilometer. In May (Figure 3 center), the maximum number of lightning days in a given place is 10 per square kilometer. The events occur on the relief and on the northeast coast of Corsica. In June (Figure 3 right), the density of sources intensifies over Corsica and over the sea, but the frequency of lightning days is much larger on the relief. We also note that the heights of occurrence of VHF sources (see panels b - or f - of each month in Figures 3, 4, 5) are increasingly high showing that the lightning events are associated with convection on the relief, also in connection with the development of the height of tropopause. In July (Figure 4 left), the density of VHF sources (panel c) is high over the northeastern half of the domain but the corresponding lightning events (panel g) occur most often over a relatively small area located in the center of the northern part of Corsica (maximum of 28 lightning days per square kilometer over the cumulative observation of July, that is to say over 186 days). In August (Figure 4 center), the spatial distribution and intensity of density (panel c) and frequency (panel g) are similar to July, with

slightly higher altitudes. The frequency of events is distributed as in July but also on the relief a little further west. In September (Figure 4 right), the number of sources (panel c) becomes important over the sea in the east of Corsica (warmer than in the west of Corsica) where the frequency (panel g) exhibits a maximum of 22 lightning days per square kilometer. This behavior illustrates a change in the meteorological regime. For the month of October (Figure 5 left), the VHF source density (panel c) remains high on most of the domain except in south-west however the corresponding events (panel g) are most often located over the sea (maximum of 18 lightning days per square kilometer). Rare are the events on the land. It is to note an anomaly in their vertical distribution characterized by a maximum of the VHF sources located at unexpected low altitudes between 5 and 6 km (see section 4). In November (Figure 5 center), the events become less frequent (panel g) but almost strong in term of VHF source density (panel c), thus reflecting the occurrence of intense events. They occur mainly on the sea, and their maximum number of sources is located at usual heights (9-10 km). The month of December (Figure 5 right) is characterized by a clear weakening of electrical activity, with a maximum frequency (panel g) of 4 lightning days per square kilometer. Most of VHF sources remain located at usual altitudes (lower than 8 km) for late fall and beginning of winter.

3.3 Monthly average trend for the entire domain

The overall observations are reported as histograms (see Figure 6) based on cumulative data. Figure 6 (top) exhibits the monthly number of lightning days over the studied domain for each year from 2014 to 2019. The additional solid line shows the monthly average of lightning days for the whole period. One can keep in mind that data corresponding to April, May June, November, December 2014 and December 2015 are not considered in this average because the network was not operational at those times. This average plot shows two main maxima: (i) in June, as expected according to the elevation of the sun in the sky and corresponding to diurnal convection, and (ii) in September, corresponding to meso-scale systems associated with synoptic flows usually encountered in the Western Mediterranean basin during fall season from September to November (Ducrocq et al., 2013).

The pattern of the monthly average of lightning days is consistent with that of the average monthly variation in the number of cloud-to-ground flashes over the Iberian Peninsula of Soriano et al. (2005) and with that of the seasonal cycle of thunderstorm occurrence over the relatively large Mediterranean basin (between 25°N and 50°N) of Galanaki et al. (2018). Both exhibit a first maximum in June, and a second maximum in late summer in August/September for Soriano et al. (2005) and in September for Galanaki et al. (2018). We note that the second maximum is more intense than the first in the climatology over the Iberian Peninsula (Soriano et al., 2005) and over Corsica (present study), while it is weaker than the first in the climatology over the extended Mediterranean basin (Galanaki et al., 2018). It is likely that the thunderstorm events of early autumn (Ducrocq et al., 2013) have a predominant influence on the Iberian Peninsula, whose electrical activity is mostly concentrated in northeastern Spain under the direct influence of the Mediterranean, and on Corsica, which is totally integrated into the western Mediterranean basin. The climatology over the Mediterranean basin of Galanaki et al. (2018) is extended to many continental regions that favor diurnal convection in June which logically should minimize the

signal in September. Referring to the mean monthly flash count reported by Poelman et al. (2016) for the whole Europe that minimizes the Mediterranean signature compared to the Galanaki et al. (2018) study, we see that the continental influence largely dominates and that the Mediterranean peak of activity in September is drowned in the monomodal distribution.

The average plot in Figure 6 (top) hides some variability from year to year however September shows a remarkable reproducibility of the number of lightning days (around 15 per month) during the whole period. We can note that 2018 was clearly productive in terms of lightning days, especially in August with an exceptional number of 28 lightning days. In contrast, 2017 was relatively poor in lightning events from May to August, i.e. during the period most conducive to diurnal convection.

Figure 6 (Bottom) reproduces the annual trend of the monthly average of lightning days, with the additional information of the mean number of VHF sources per lightning day over the whole domain (min. value: 11 738 VHF sources/day in December; max. value: 1 132 263 VHF sources/day in August). April and December correspond to relatively low numbers of lightning days and simultaneously low number of VHF sources per lightning day. From May to November, the average monthly number of lightning days is higher than 10, with however a low average number of VHF sources per lightning day in May compared to the months from June to November. Therefore, April, May and December correspond to lightning events weakly active and/or weakly developed, while the events with the strongest electrical activity are encountered in August.

3.4 Hourly trends of lightning day distribution

The geographical distribution of the areas most frequently impacted by total flash activity is largely dominated by convective events over landforms (Figures 2c and 2g). It is therefore expected that this distribution is predominantly influenced by diurnal convection. To verify this, hourly distribution maps of the number of lightning days per square kilometer were plotted. The most significant maps are shown in Figure 7 between 10:00 UTC and 16:00 UTC. Before and after these times (not shown in Figure 7), the hourly distribution shows low values everywhere but with more frequent activity over the sea, especially off the east coast side from 00:00 to 08:00 UTC. Barthlott et al. (2016) numerically identified two possible mechanisms initiating nocturnal offshore convection in the East of Corsica by (i) low level convergence due to the interaction between katabatic flow from the relief and the synoptic flow over the sea and (ii) lee-side convergence due to the island barrier effect.

On the other hand, we can clearly see an increase in the number of days of lightning per square kilometer between 10:00 and 11:00 above the relief near the northeast coast. From 11:00 UTC to 12:00 UTC, the area of most frequent lightning activity extends to all the reliefs, with a much localized maximum above the crossroads of the three large valleys, near the area where the density of global VHF sources is maximum (see Section 3 and Figure 2c). Between 12:00 UTC and 13:00 UTC, the daytime flash frequency reaches its maximum above the North-East center mountainous region (Castagniccia). This region is by far the most frequently affected by lightning activity in the middle of the day. After 13:00 UTC, the highest

frequencies of the number of lightning days decrease while being always located on all the reliefs but with gradually a small displacement towards the Northeast of Corsica (i.e. downwind which is often from the southwest as seen in section 3.3 and Figure 2g). This displacement overflows on the sea between 14h00 UTC and 15h00 UTC. Between 15h00 UTC and 16h00 UTC, the lightning activity disappears from the Castagniccia and remains a little more frequent on the Western relief and at sea near the North-East coast.

3.5 Monthly altitude distribution of VHF sources

The altitude histograms displayed in Figure 2b or 2f gather all observed events since 2014. When each month of the year is studied separately (Figure 3, 4, 5), these histograms provide information on the average evolution of thunderstorm cell development over the year. The comparison between all these monthly altitude histograms is proposed in Figure 8, separating the months of April to August on one side (Figure 8 left) and the months of August to December on the other (Figure 8 right). The histogram for August is displayed in Figures 8 left and right as a reference. From April to August, the general trend is on the one hand an increase in the number of VHF sources whatever the altitude, and on the other hand a shift towards the high altitudes of the maximum number of VHF sources. This observation indicates that from April to August, on the one hand, the electrical activity on the domain increases, on the other hand, its vertical development is increasingly high. This vertical development follows the seasonal evolution of the tropopause. From August to December, the opposite behavior is observed with a decrease in the number of VHF sources whatever the altitude - except for the month of October below 7 km altitude - and a decrease in the altitude of the maximum number of VHF sources - except for the month of November because of the very peculiar behavior of the month of October.

Unexpectedly, October is characterized by a maximum number of VHF sources located at an altitude between 5 and 6 km abnormally low compared to the altitude histograms of other months (between 7 and 10 km). The review of the 76 thunderstorm events from October 2014 to 2019 (see Figure 9) allowed us to identify 2 very huge events that produced 13.2 million VHF sources (14/10/2016, https://saetta.aeris-data.fr/quicklooks/#/day/2016-10-14) and 16.3 millions VHF sources (29/10/2018, https://saetta.aeris-data.fr/quicklooks/#/day/2018-10-29), to be compared to the 3rd most important event which produced only 3.1 million VHF sources. The appearance of the altitude histogram in October is thus mainly due to these two intense events. Without these two intense events, the trend of decreasing activity and altitude of lightning persists from August through December (Figure 8b).

4. Specific results

4.1 Negative dipoles

Not presented here, a detailed manual analysis on a flash-by-flash basis of SAETTA data of both huge events (14/10/2016 and 29/10/2018) responsible for the vertical distribution anomaly of the VHF sources in October (see Section 3.5) showed that the thunderstorm cells were characterized by a zone of negative charge at the top and a zone of positive charge at the

bottom, that is to say by what is called a negative dipole compared to the usual tripole structure of a thunderstorm cloud with a zone of positive charge at the top and a zone of negative charge at mid-height and a secondary positive pole at low level.

An example of negative dipole is shown in Figure 10 (10/08/2017, Figure 10 top) and compared to a more usual positive dipole event (15/10/2019, Figure 10 bottom) with about the same general characteristics, namely relatively small cells moving in a southwesterly flow and few VHF sources at the upper level (about 9 km altitude), and many VHF sources at the mid-troposphere level (about 5 km altitude) according to the vertical histograms in Figure 10. However, two details allow to differentiate their electrical structures: (1) the flashes of the negative dipole are intra-cloud flashes propagating over the whole thickness of the cloud (see altitude vs. time panel) while those of the positive dipole exhibit mostly a weak vertical development at low level (probably CGs) with only 3 IC flashes developing over the whole thickness of the cloud hence inducing a low number of VHF sources around 9 km (see altitude vs. time panel); and (2) the diagnosis of the power with which the VHF sources are detected (Figure 10 right) clearly shows that for the negative dipole (Figure 10j top) this power is weak at the upper level (blue color, positive discharge propagating in a zone of negative charge) and strong at the lower level (green color, negative discharge propagating in a zone of positive charge), meanwhile for the positive dipole (Figure 10j bottom) this power is strong at the upper level (negative leader propagating in a zone of positive charge) and weak at the lower level (positive leader propagating in a zone of negative charge).

The cloud systems concerned are very different from supercellular systems with inverted polarity observed in the US Great Plains (Lang et al., 2004; Rust et al., 2005; Tessendorf et al., 2007; MacGorman et al., 2008). On the other hand, Chmielewski et al. (2018) documented several single-cell and multicell storms with anomalous charge structures characterized by a primarily positive charge at midlevels (cf. Figure 1b). In the present study, the SAETTA 3D mapping shows that the negative dipoles are characterized by a moderate vertical development, a relatively weak horizontal extension of about ten kilometers and move in a quasi rectilinear way on distances being able to reach 230 km with rather fast speeds ranging between 80 and 90 km/h on average and up to more than 100 km/h for some of them (speed calculated from the SAETTA observations). For example, the sequence displayed in Figure 10d top corresponds to a speed of 118 km/h calculated from the distance between the vertical channels of the 1st and last flashes of the sequence divided by the duration between the dates of these 1st and last flashes.

4.2 African dust influence?

One can point out that both huge events of October (14/10/2016 and 29/10/2018) are also characterized by a strong southerly flow, which is associated with an important transport of desert dust from Africa. This is easily identifiable with the visualization tool available on earth.nullschool.net with a display of the wind at 850 hPa and a background color corresponding to the AOT Dust (Appendix A3 and Appendix A4, where AOT Dust and wind direction are equal to 0.745 and 175°, and to 0.618 and 170°, respectively). The observation of African dust presence can be made for the negative dipole of Figure 10 top (10/08/2017, AOT Dust = 0.149, wind direction at 850 hPa = 235°), but not for the upper positive dipole of

Figure 10 bottom (15/10/2019, AOT Dust = 0.080, wind direction at 850 hPa = 225°). Concerning the latter, the upstream flow does not come from Africa but from the Atlantic Ocean through Spain and northwestern Mediterranean basin.

The question of the influence of African dust to the thunderstorm development thus arises. To address this issue, the whole dataset of thunderstorm days has been explored and characterized from the point of view of the aerosol context and of the influencing atmospheric fluxes. 29 negative dipole events have been identified, most of them less intense than the two October events mentioned above. Figure 11, which gathers the information for the whole set of thunderstorm events, shows that the negative dipole cases (red, orange and yellow spheres) occur in a highly aerosol-laden atmospheric context (AOT Dust or total AOT > 0.2) and in a south to southwest flow sector (wind direction at 850 hPa between 160° and 250°). The yellow spheres of arbitrary size and orange ones highlight the desert dust context with strong AOT Dust. The large sizes of the orange spheres show that the GEOS5 and CAMS data are consistent with the in-situ AERONET photometric data in terms of the strong presence of aerosols belonging to the coarse mode of atmospheric aerosol populations (dust type). The large diameter red spheres show very high total AOT values and a low contribution of the fine mode of aerosols, thus reinforcing the observation of a strong loading of the atmosphere with large aerosols. It can be noted that one lightning event with negative dipole comes out of this trend, showing an incident wind direction at 850 hPa from the East (yellow sphere, AOT Dust = 0.638, wind direction = 95°). After analysis, this event of 22/04/2019 remains well in a context of desert dust which crossed the Mediterranean basin by southern flow coming from Libya, and which was gradually advected on Corsica by an eastern flow. It can also be pointed out that some positive dipole events occurred with winds in the 210°-260° sector and with a non-negligible dust AOT or total AOT ranging from 0.2 to 0.3. However, the small size of the corresponding blue spheres shows that the aerosols concerned belonged mainly to the fine mode.

4.3 June 2019: aerosol and meteorological context analysis

One month in particular was very rich in negative dipole lightning events. In fact, June 2019 had 8 negative dipole events out of 9 thunderstorm episodes, which makes June 2019 stand for 27,6 % of the 29 negative dipole events over the whole studied period (dots with warm colours in Figure9 and dates of negative dipole events in Appendix 5 Table A5). Figure 12 provides the aerosol context and the influencing atmospheric fluxes for all days in this month of June 2019 (including days without thunderstorms). The 8 negative dipole events all correspond to a wind direction close to the south (200°) and to an AOT Dust higher than the monthly average. That is to say that they are all formed by southern flow with transport of Saharan dust. As for the 9th day of storm, the wind direction and AOT Dust are very different and the storm has a regular electrical structure. It seems therefore that there is a strong correlation between the formation of negative dipoles and the presence of Saharan dust particles.

On the other hand, we explored in detail the prevailing meteorological context during these 9 thunderstorms events of June 2019 in order to identify possible dynamic and thermodynamic ingredients specific to the formation of such negative dipole thunderstorms. The objective was to characterize the large scale meteorological context associated to each of them. We will

first do a detailed analysis for one specific and interesting stormy night (June 9-10), then expand to all other negative dipole events.

Specific case of the 9-10th of June night: in the Figures 13 and 14 we present the synoptic situation for the event that occurred during the night from the 9 to 10th of June. The ARPEGE run from midnight is used as an analysis of the situation. Figure 13 shows the geopotential and temperature (ZT500) field the 10/06/2019 at 00 UTC: geopotential height, temperature and wind barbs display a SSW flux due to the presence of a deep trough from Ireland to Morocco. On Figure 14 we display the surface situation (MSLP and the wet bulb potential temperature, θ'w at 850 hPa level) for the same night at same hour: a flat low is present above the entire Mediterranean sea, values of θ'w are normal over the gulf of Genoa. Figure 15 shows infrared (10.8 GHz) Meteost Second Generation (MSG) measurements à 01:00 UTC together with Radar reflectivities and cloud-to-ground strikes (red triangles). These pictures show (i) a top cloud temperature around -60 °C, which – crossed with Figure 16 emagram - means that the top altitude is on the profile inversion and that there is no overshooting top, and (ii) that precipitations and electrical activity are not intense. These figures give us some general information: (i) the global flow of the mid altitude layers is southwesterly; (ii) convection takes place in the eastern region of a trough, where ageostrophic horizontal winds are known to diverge and to be source of upstream winds (Holton and Hakim, 2005, chapter 6); and (iii) no PV forcing are involved in the convection. To complete the meteorological analysis, we should assess the tropopause configuration: a PV forcing (not shown) is present from the west of France to Iberic Peninsula, but far from Corsica and gulf of Genoa. We can therefore suppose that this forcing had no effect on convection for this situation.

The 1.3 km scale AROME model was used to identify convection origin at lower scale. We selected the AROME run simulating the total reflectivities (due to simulated rain) the closest to the one observed by the French precipitation radar system. We then have made temperature profiles in simulated convective clouds. Figure 16 shows a vertical profile corresponding to the same situation (10/06/2019 at 22H00 UTC using the AROME run of 18H00 UTC). It shows an inverted temperature profile near the ground, overhang by a very dry layer from 970 hPa to 700 hPa. Even if the profile is unstable, such a dry and thick layer avoids convection from the surface; only convection from the 700 hPa layer can take place where humidity is sufficiently high. This is the case of elevated convection that occurs above the boundary layer (Corfidi et al. 2008). This profile is very close to the observations one hour later (Ajaccio radiosounding not shown).

We suggested in previous paragraphs that the negative dipole configuration could be linked to the presence of desert dust in upper air. We have just shown that these events were observed when the mid-altitude flux was between 160° to 250°, suggesting that air particles origin could be Sahara. We investigated this hypothesis using the HYSPLIT tool developed by NOAA and available online (Stein et al. 2015). By considering two localizations and 3 levels (2500, 3200 and 4000 meters high) we simulated the backward trajectories of these particles using the GFS model. The vertical profile shown in Figure 16 leads to the hypothesis that convection arises in the 700 hPa layer; this level corresponds to the 3200 meters height and justifies the choice to compute backward trajectory at the 3200 m level. Results are shown in Figure 17 and clearly suggest that all mid-altitude particles were above the Saharian desert 2 and 3 days before. Some of them could even be originally

present just above the surface: red and blue curves are close to the 500-meter level between 2 and 3 days before. This may support that air particles are full of desert dust.

All June 2019 events synthesis: the same analysis was done for each stormy day of June 2019. The Table 1 shows a synthesis of this analysis for each of the 7 events (9 days involved). We reported the presence of negative dipole, the direction of the mid-altitude flux, the MSLP conditions, the presence or not of a PV forcing near the Corsica island and the gulf of Genoa and finally if it is elevated convection. All these events were associated with southwesterly mid-altitude flow above a flat low around the Corsica Island. No PV forcing was identified except for the 21-22th event. All negative dipole events of June 2019 corresponded to elevated convection. Moreover the HYSPLIT NOAA tool was used for all June events. Once again a strong similarity was shown between all of them. At the altitude where elevated convection is triggered, all air parcels were coming from the Sahara. At lower altitude, the origins where sometimes very different (Spain, Central Europe, Mediterranean Sea). Hypotheses concerning the role of African dust in the electrification of these events will be addressed in the following section.

5. Discussion

The 6-year LTO of the number of lightning days (Figure 2g) clearly show that lightning activity over Corsica occurs most often over the main reliefs, with some relatively frequent events over the sea in the northeast region of the domain and to a lesser extent near the southeast coast of Corsica. However, the hourly activity (Figure 6) confirms that this activity is maximal between 11:00 UT and 14:00 UT, i.e. it originates from the typical diurnal convection. Moreover, Figure 3 right side, and Figure 4 left side and center show that the months of June, July and August are the months that most clearly influence this climatology.

Comparing Figures 4g center and 5g left side, we see that August and October are characterized by almost completely opposite lightning day distributions. Lightning activity occurs most often over Corsica in August and most often over the sea in October. When looking at the corresponding VHF source density distributions (Figures 4c center and 5c left side), this behavior does not seem obvious. The reason is that rare but very active events occur over the sea in August and over Corsica in October. August is also characterized by a distribution of VHF sources with relatively sharp contours (Figure 4c center), while in October these contours are relatively diffuse and widespread, typical of moving cloud systems (Figure 5c left side). Furthermore, both months exhibit almost the same average number of lightning day (Figure 6 bottom), i.e. 11.0 in August and 12.7 in October. Yet, Scheffknecht et al. (2017) have shown that the corresponding heavy precipitations are much more intense in October than in August. These comparisons highlight the difference in regime between these two months, with mainly diurnal convection in August and the presence of organized convective systems in October. Beyond the dynamic and microphysical characteristics that can explain the higher precipitation production in October, the duration of storm events is obviously a key parameter. For example during the most active year of 2018, the average daily duration of electrical activity

(a proxy of the duration of storm activity over the domain) - simply estimated from the start time to the end time of the total electrical activity of all thunderstorms considered over the entire domain - is about 5 hours in August and 11 hours in October. This should support more precipitation production in October.

Another feature of the lightning climatology that confirms the preliminary observations of Coquillat et al. (2019) is the presence of a strong local maximum of VHF sources in a micro-region located at the convergence point of the 3 main valleys of Corsica in the northern center of the island (Figure 2c). This area is also quite often the seat of convection (Figure 2g) and especially between 11:00 and 14:00 UT, we can reasonably say that it favors the intense daytime convection. A more detailed analysis of the monthly distributions of VHF sources (Figures 3c right side and Figure 4c left side and center) shows that this micro region is particularly active in June, July and August, with perhaps a greater regularity in July (Figure 4g left side). Tidiga et al (2018) showed that convection in this area could be favored by the convergence of low layer flows of moist air from sea breezes channeled through these 3 main valleys.

Counting the number of days a thunderstorm hits the island each year from 2015 to 2019 (omitting the all-too-short year 2014, which underestimates the annual total), one finds an average annual number of lightning days over Corsica alone of about 78 (over 103 on the studied domain). This number is minimal since the months of January to March are not taken into account in this calculation because the corresponding data are either unavailable or too fragmented due to the wintering of high mountain stations. If we compare this number of 78 annual lightning days for an island of 8740 km^2 with the results of Figure 4 of Williams et al. (2004), we can say that Corsica is among the most electrically active islands, which is probably due to its high relief. Furthermore according to Williams et al. (2004), Corsica must exhibit a more continental than maritime behavior. As emphasized by them, the continental behavior should also be driven by the boundary layer aerosol concentration. We have seen in section 4 that aerosols can have a clear impact on lightning activity, but surprisingly if we refer to the study of Williams et al. (2004), it is not on the continental area but on the maritime area that this influence acts most in the case of Corsica, and with a source of aerosols not endogenous but exogenous, and coming from Africa. This type of behavior could also be found in the lightning events observed in Catalonia (Salvador et al., 2021).

The unexpected observation we made with SAETTA is that of anomalously electrified thunderstorms that until then were usually known to be most often produced in supercellular systems such as those frequently observed in the US Great Plains (Lang et al., 2004; Rust et al., 2005; Bruning et al., 2007; Tessendorf et al., 2007; MacGorman et al., 2008, Stough et al., 2021). However Chmielewski et al., (2018) have reported some single-cell and multicell anomalously electrified storms. They considered that dry air entrainment could promote positive charging of graupel at low temperatures by increasing the proportion of small cloud droplets in the mixed phase layer where the noninductive charging process acts. In the present case of the 8 negative dipole events of June 2019 for which the meteorological context has been analyzed, convection were triggered at about 700 hPa in layers that usually contain much less water vapour than surface layer, and above a very dry layer even though the events occurred in a maritime environment. Moreover all the negative dipoles observed by SAETTA

are associated with a very specific aerosol environment. In such a way that we are in the presence of meteorological objects that could provide interesting answers in the future on the involvement of aerosols in the electrification of clouds.

The present results show a very strong correlation between the appearance of cloud systems with a negative electric dipolar structure, and the presence of large quantities of coarse dust aerosols from the African continent. This correlation does not imply a cause-effect relationship, but it allows us to characterize the environment in which these anomalous cloud structures develop. The question of the influence of aerosol on cloud physics is not straightforward. Rosenfeld et al. (2008) proposed a conceptual model of a convective cloud fed with Cloud Condensation Nuclei (CCN) by polluted surface air, in which precipitation formation is delayed by the presence of small liquid water droplets formed on the many CCN. These droplets are transported higher to the supercooled levels where they freeze on the ice crystals. The release of latent heat induced by this phase change at higher altitudes thus corresponds to a greater upward heat transport that reinforces convection. They also discussed the relative impacts of the radiative and microphysical effects of aerosols, the former representing a factor limiting convection by reducing the contribution of solar radiation to the ground.

In the present case of convective clouds exhibiting a negative dipolar structure in southern flows of African dust aerosols, the vertical development does not seem to be reinforced compared to the usual events in the absence of African dust aerosols. Moreover, the aerosols concerned are not of anthropogenic origin and do not come from the lower layers. Additionally, elevated convection is triggered above a relatively warm and dry atmospheric boundary layer (at least in all cases of June 2019), so the cells are effectively fed by these desert dusts and convection is not closely related to thermal conditions on the ground. We are therefore in the presence of a configuration that does not fit the conceptual model of Rosenfeld et al. (2008). It can be noted that the large atmospheric optical thickness is expected to significantly limit solar radiation to the ground, which is consistent with the relatively low surface temperature resulting in a high Convective INhibition (CIN) as seen in the emagrams of the June 2019 negative dipole events (e.g. in Figure 16).

The question that arises is: how can the African dust aerosols (which we do not know if they are efficient CCN and even Ice Nuclei (IN) or not) and the meteorological environment (characterized by a strong CIN, a warm and dry atmospheric boundary layer, and an elevated convection triggering) lead to a polarity inversion? Let us assume that a positive dipole corresponds to an intermediate cloud LWC (e.g. from about 1 to about 3 g m^{-3}, see Section 1) in the mixed phase region where the non-inductive charging process acts. In the case of the present negative dipole events, the strong presence of desert dust and/or the particular meteorological conditions of convection triggering in mid altitudes probably lead to cloud LWC either weaker or stronger than these intermediate values, imposing the acquisition of a positive charge to the graupel (Takahashi, 1978; Saunders, 2008). What are then the processes that act and how?

It appears that there may be several competing processes: (i) if the aerosols present are effective CCN, the multiplication of supercooled water droplets can promote a high LWC in the mixed phase zone; (ii) if the aerosols present are not effective CCN or, on the contrary, effective IN, the LWC in the mixed phase zone will be low to the benefit of the presence of many

ice crystals, provided that the temperature conditions allow the activation of the IN; (iii) if the triggering of convection in mid altitudes is confirmed for all the events of negative dipole on Corsica, the storm cell is fed with an air relatively poor in water vapor (the water vapor content of the atmospheric air decreases with altitude as one rises far from the sources of evaporation) so the LWC in the mixed phase zone is necessarily low; and (iv) if process (iii) is confirmed, process (i) will be modulated by the smaller size of the supercooled water droplets that share the little water vapor present, so the LWC in the mixed phase zone will be consequently low. These hypotheses tend mainly towards low LWC in the mixed phase region of the cloud, which is probably induced by a low water vapor content that seems to be a key parameter. The relatively low vertical development of the storm cells concerned (satellite images as in Figure 15) is consistent with this hypothesis since a low water vapor content induces a low amount of latent heat released by condensation.

Generally, anomalous charge structures are favored in a context of high LWC riming that supports positive charging of graupel (Saunders, 2008). For instance, Chmielewski et al. (2018) have suggested that dry air entrainment in several single-cell and multicell storms with anomalous charge structure would enhance the proportion of droplets in the mixed phase region by limiting the growth of precipitation sized particles through evaporation. This promotes the positive charging of graupel by an increase in LWC. Stough et al. (2021) have analyzed supercellular thunderstorms with anomalous electrical structure. They hypothesized that dry air may have instead reduced the superpersaturation with respect to ice, leading to an increased magnitude of the positive charging of graupel for a given LWC, as shown from an experimental and modeling point of view by Berdeklis and List (2001) and Mitzeva et al. (2005), respectively. Indeed during the non inductive charging process involving graupel and ice crystals, faster growing ice surface will charge positively according to Saunders (2008), i.e. positive graupel in case of lower supersaturation with respect to ice crystals. In present study, dry entrainment has not been documented for the 8 negative dipole events for which the meteorological environment has been analyzed. However, the convection was driven by air containing relatively little water vapor compared to a normal event. Thus, the hypothesis of a strong LWC to explain this loading anomaly is unlilkely. The limitation of superpersaturation with respect to ice seems a more likely explanation.

Another point that raises questions is that of the African dust aerosols themselves, which, by impact or friction between them, could possibly carry an electrical charge. Should this be the case, what would be the influence of the proper charge of the numerous aerosols on the cloud electrification processes? This question remains open in the absence, at first, of available in situ measurements of their electric charge and of laboratory studies of water/ice condensation on initially charged particles.

6. Conclusions and perspectives

Three-dimensional lightning observations using the SAETTA network of LMA stations have enabled accurate mapping of total lightning activity over Corsica between 2014 and 2019. This is the first time that such long-term 3D observations have

been produced. The depth of the data in terms of years is not sufficient to extract reliable inter-annual trends since over a 6-year period, the variability of the signal outweighs any trend. However, the observations provide a good description of the type of lightning events occurring in Corsica according to the months of the year, a precise location of the most affected regions, and the most productive hourly period. Different characteristics were identified as follows:

1- The general pattern of lightning activity is thus characterized by a maximum of activity on the relief in June, which corresponds to the expected behavior of diurnal convection on an island of large dimensions. A second maximum of activity of greater amplitude and associated with a more homogeneous activity from one year to another is located in September. The lightning events concerned are mostly organized convective systems associated with the dynamics at larger scale, and are located mainly on the east coast of Corsica and at sea with a notable recurrence in the northeast of the area between the long cape in the North of Corsica and Italy

2- The accumulation of all the lightning activity over the 6-year period shows however the major role of the Corsican relief on the recurrence of thunderstorm days. Moreover, if we consider the activity in terms of number of VHF sources, which represents a kind of proxy of the intensity of this activity, a micro-region located at the crossroads of the 3 main valleys (approximate coordinates on the map in Appendix A1: +10 km West-East and +12 km South-North) is the place of a very pronounced maximum of activity. This maximum is particularly fed by diurnal convection events in June, July and August between 11:00 and 14:00 UTC. The strong convergence of low level flows of moist air coming from sea breezes channeled by these three valleys which meet there is supposed to be at the origin of this maximum activity.

3- The information on the altitude of VHF sources also allows us to characterize the evolution of the electrical structure of thunderstorm systems over the months. It has been shown that this structure is on average characterized by a layer centered near the tropopause (10 km in August) showing strong electrical activity associated with negative leader propagating in positive cloud charge carried mostly by ice crystals, and by a layer centered at mid-troposphere (6.5 km in August) showing weaker electrical activity associated with positive leaders propagating in negative cloud charge mainly carried by graupel (Ribaud et al., 2016). The altitude of these layers increases from spring to August and then decreases.

4- The occurrence of storm systems characterized by an anomalous charge structure of negative dipole type, i.e. consisting of a layer of negative charge on top of a layer of positive charge, has been highlighted thanks to the vertical profiles of VHF sources. An exhaustive analysis of all the events observed over the 6-year period has allowed us to identify the meteorological characteristics and aerosol environments associated with these negative dipole events. All correspond to flows coming mainly from the South and carrying large amounts of dust of African origin, characterized by high optical thickness and relatively large particle sizes. A more detailed study of the meteorological conditions in June 2019, during which 8 of the 9 lightning events that occurred were negative dipoles, also highlighted the very particular atmospheric conditions during these events. These conditions are

characterized by a very dry boundary layer with a temperature inversion, thus significant CIN energy, and the triggering of convection above the boundary layer in mid altitudes at around 700 hPa.

To explain why the observed storm systems present a negative dipole structure due to the aerosol environment and/or due to the meteorological conditions mentioned above is a challenging question. The chain of processes involved (dynamic, thermodynamic, microphysical, electrical) is indeed complex and the ability of African dust aerosols to act as condensation nuclei or as ice nuclei is unknown. Based on the hypothesis of the predominance of the non-inductive charging process and on the results of laboratory experiments (see Saunders, 2008), it seems that the hypothesis of the presence of a very low cloud LWC in the mixed phase region is the most tempting. Indeed, in the case of very low LWC - probably exceptional - the experimental results synthesized by Saunders (2008) in his Figure 12 show that the graupel remains positively charged even at low temperature. This is the case for all the curves in this Figure 12 except for the curve of Saunders and Peck (1998) for which the experimental conditions were different, as highlighted by Pereyra et al. (2000). One can also see the Figure 8 of Takahashi (1978). A very low LWC would be due on the one hand to the relatively low content of water vapor related to the mode of initiation of elevated convection above 700 hPa. On the other hand, if the aerosols are good IN, the ice crystals will multiply at the expense of the liquid water cloud droplets, whereas if they are good CCN, the multiplication of the liquid water droplets may not allow to obtain a sufficient cloud water content because of the low initial water vapor content.

The negative dipole events observed in Corsica, which present very specific characteristics and which develop in an original environment under the influence of African dust, are interesting objects which prompt us to question the microphysical and electrical processes that act within thunderstorm cells. To answer these questions, in situ observations/measurements of cloud microphysics, cloud LWC, water vapour content, aerosol environment, and aerosol properties - especially solubility - would be essential. Moreover, it is not forbidden to imagine that the African dust aerosols could possibly be initially electrically charged either during their formation or during their transport by shocks between particles. In this case, there could be an additional unknown influence of the initial electric charge of the aerosols on the microphysical processes leading to the formation of the drops and ice crystals and to the electric charge carried by each hydrometeor. Measurement of the aerosol electrical charge as well as laboratory experiments of supercooled water droplet and ice crystal growth on electrically charged CCN and IN may be required.

It would be appropriate to verify first that all the negative dipole events in Corsica, concerned by the African dust, correspond to the triggering of elevated convection. We could also integrate a background aerosol statistic by identifying the nature of the most influential/implicated aerosols at the climatological scale (dust, pollution aerosol, PM2.5, PM10, CO tracer, marine aerosol). This questioning could possibly be addressed through modeling via sensitivity studies on microphysical and aerosol schemes. Thus, many questions remain to be explored regarding these events, with a good prospect of analyzing small-scale processes involving aerosol particles, cloud microphysics, and electrification processes. The interactions between storm clouds and aerosols are the subject of additional studies thanks to the observations made during the EXAEDRE campaign (https://anr.fr/Projet-ANR-16-CE04-0005).

Acknowledgments: We thank the AERONET-PHOTON PI (P. Goloub) and the Plateforme CORSiCA d'Observations Atmosphériques (PCOA, https://corsica.obs-mip.fr/) for their effort in establishing and maintaining Ersa site. Acknowledgements are also addressed to SAETTA main sponsors: Collectivité Territoriale de Corse through the Fonds Européen de Développement Régional of the European Operational Program 2007–2013 and the Contrat de Plan Etat Région that funded the CORSiCA project; Collectivité de Corse through the CORSiCA 2017–2019 project; CNRS-INSU through the HyMeX/MISTRALS program; ANR IODA-MED; CNES through the SOLID project; UPS/Observatoire Midi-Pyrénées; and Laboratoire d'Aérologie. We also sincerely thank the many individuals and regional institutions in Corsica (including the Conservatoire du Littoral, Qualitair Corse, and INRA San Giuliano), who host the 12 stations of the network, who helped us to find sites, or who bring us assistance for the logistics during field missions.

References

Adler, B., Kalthoff, N., Kohler, M., Handwerker, J., Wieser, A., Corsmeier, U., Kottmeier, C., Lambert, D., Bock, O., 2016. The variability of water vapour and pre-convective conditions over the mountainous island of Corsica, Q. J. R. Meteorol. Soc., 142 (Suppl 1), 335–346, DOI:10.1002/qj.2545.

Anderson, G., Klugmann, D., 2014. A European lightning density analysis using 5 years of ATDnet data. Nat. Hazards Earth Syst. Sci. 14, 815–829. https://doi.org/10.5194/nhess-14-815-2014.

Banta, R. M., 1990. The role of mountain flows in making clouds, In: Blumen W.: Atmospheric processes over complex terrain, Meteor. Monogr., 45, 229–283.

Barthlott, C., Kirshbaum, D. J., 2013. Sensitivity of deep convection to terrain forcing over Mediterranean islands, Q. J. R. Meteorol. Soc., 139, 1762–1779, doi: 10.1002/qj.2089.

Barthlott, C., Adler, B., Kalthoff, N., Handwerker, J., Kohler, M., Wieser, A., 2016. The role of Corsica in initiating nocturnal offshore convection, Q. J. R. Meteorol. Soc., 142 (Suppl 1), 222–237, DOI:10.1002/qj.2415.

Boccippio, D. J., Cummins, K. L., Christian, H. J., & Goodman, S. J., 2001. Combined satellite- and surface-based estimation of the intracloud-cloud-to-ground lightning ratio over the Continental United States. Monthly Weather Review, 129(1), 108–122. https://doi.org/10.1175/1520-0493(2001)129<0108:CSASBE>2.0.CO;2.

Bruning, E. C., Rust, W.D., Schuur, T. J., MacGorman, D. R., Krehbiel, P. R., Rison, W., 2007. Electrical and polarimetric radar observations of a multicell storm in TELEX, Mon. Weather Rev. 135, 2525–2544, doi.org/ 10.1175/MWR3421.1.

Bruning, E. C., Weiss, S. A., Calhoun, K. M., 2014. Continuous variability in thunderstorm primary electrification and an evaluation of inverted-polarity terminology, Atmos. Res., 135–136, 274–284, doi.org/10.1016/j.atmosres.2012.10.009.

Caumont, O., Mandement, M., Bouttier, F., Eeckman, J., Lebeaupin Brossier, C., Lovat, A., Nuissier, O., Laurantin, O., 2021. The heavy precipitation event of 14–15 October 2018 in the Aude catchment: a meteorological study based on operational numerical weather prediction systems and standard and personal observations, Nat. Hazards Earth Syst. Sci., 21, 1135–1157, doi.org/10.5194/nhess-21-1135-2021.

Chen, Y.-C., Wang, S.-H., Min, Q., Lu, S., Lin, P.-L., Lin, N.-H., Chung, K.-S., Joseph, E., 2021. Aerosol impacts on warm-cloud microphysics and drizzle in a moderately polluted environment, Atmos. Chem. Phys., 21, 4487–4502, doi.org/10.5194/acp-21-4487-2021.

Chmielewski, V. C., and Bruning, E. C., 2016. Lightning Mapping Array flash detection performance with variable receiver thresholds. J. Geophys. Res. Atmos.,121, 8600–8614,doi:10.1002/2016JD025159.

Chmielewski, V. C., Bruning, E. C., & Ancell, B. C., 2018. Variations of Thunderstorm Charge Structures in West Texas on 4 June 2012. Journal of Geophysical Research: Atmospheres, 123(17), 9502–9523. https://doi.org/10.1029/2018JD029006.

Corfidi, S. F., Corfidi, S. J., Schultz, D. M., 2008. Elevated convection and castellanus: ambiguities, significance and questions, *Weather and Forecasting*, *23*(6), 1280-1303.

Dubovik, O., Sinyuk, A., Lapyonok, T., Holben, B. N., Mishchenko, M., Yang, P., Eck, T. F., Volten, H., Munoz, O., Veihelmann, B., van der Zande, W. J., Léon, J.-F., Sorokin, M., Slutsker, I., 2006. Application of spheroid models to account for aerosol particle nonsphericity in remonte sensing of desert dust, J. Geophys. Res., 111, doi:10.1029/2005JD006619.

Ducrocq, C., Braud, I., Davolio, S., Ferretti, R., Flamant, C., Jansa, A., Kalthoff, N., Richard, E., Taupier-Letage, I., Ayral, P.-A., Belamari, S., Berne, A., Borga, M., Boudevillain, B., Bock, O., Boichard, J.-L., Bouin, M.-N., Bousquet, O., Bouvier, C., Chiggiato, J., Cimini, D., Corsmeier, U., Coppola, L., Cocquerez, P., Defer, E., Delanoë, J., Di Girolamo, P., Doerenbecher, A., Drobinski, P., Dufournet, Y., Fourrié, N., Gourley, J. J., Labatut, L., Lambert, D., Le Coz, J., Marzano, F. S., Molinié, G., Montani, A., Nord, G., Nuret, M., Ramage, K., Rison, B., Roussot, O., Said, F., Schwarzenboeck, A., Testor, P., Van-Baelen, J., Vincendon, B., Aran, M., Tamayo, J., 2014. HyMeX-SOP1, the field campaign dedicated to heavy precipitation and flash-flooding in the northwestern Mediterranean, Bull. Am. Meteorol. Soc., 95, 1083-10.1175/bams-d-12-00244.1.

Emersic, C., Saunders, C. P. R., 2010. Further laboratory investigations into the Relative Diffusional Growth Rate theory of thunderstorm electrification, Atmos. Res., 98, 327-340.

Enno, S-E. Sugier, J. Alber, R., Seltzer, M., 2020. Lightning flash density in Europe based on 10 years of ATDnet data. Atmos. Res., 235, 104769. https://doi.org/10.1016/j.atmosres.2019.104769.

Flamant, C., Chaboureau, J.-P., Chazette, P., Di Girolamo, P., Bourrianne, T., Totems, J., Cacciani, M., 2015. The radiative impact of desert durst on orographic rain in the Cévennes-Vivarais area: a case study from HyMeX, Atmos. Chem. Phys., 15, 12231-12249.

Fuchs, B. R., Rutledge, S. A., Bruning, E. C., Pierce, J. R., Kodros, J. K., Lang, T. J., MacGorman, D. R., Krehbiel, P. R., Rison, W., 2015. Environmental controls on storm intensity and charge structure in multiple regions of the continental United States, J. Geophys. Res. Atmospheres, 120(13), 6575–6596, doi.org/10.1002/2015JD023271.

Fuchs, B. R., Bruning, E. C., Rutledge, S. A., Carey, L. D., Krehbiel, P. R., & Rison, W., 2016. Climatological analyses of LMA data with an open-source lightning flashclustering algorithm. Journal of Geophysical Research: Atmospheres, 121, 8625–8648. https://doi.org/10.1002/2015JD024663.

Fuchs, B. R., & Rutledge, S. A., 2018. Investigation of lightning flash locations in isolated convection using LMA observations. Journal of Geophysical Research: Atmospheres, 1–17. https://doi.org/10.1002/2017JD027569.

Galanaki, E., Lagouvardos, K., Kotroni, V., Flaounas, E., Argiriou, A., 2018. Thunderstorm climatology in the Mediterranean using cloud-to-ground lightning observations. Atmos. Res. 207, 136–144. https://doi.org/10.1016/j.atmosres.2018.03.004.

Holton, J. R., Hakim, G. J., 2013. An introduction to dynamic meteorology, Waltham, MA.

Jayaratne, E. R., Saunders, C. P. R., Hallett, J., 1983. Laboratory studies of the charging of soft-hail during ice crystal interactions, Q. J. R. Meteorol. Soc., 109, 609-630.

Kalthoff, N., Adler, B., Barthlott, C., Corsmeier, U., Mobbs, S., Crewell, S., Träumner, K., Kottmeier, C., Wieser, A., Smith, V., Di Girolamo, P., 2009. The impact of convergence zones on the initiation of deep convection: A case study from COPS, Atmos. Res., 93, 680-694.

Kalthoff, N., Adler, B., Wieser, A., Kohler, M., Träumner, K., Handwerker, J., Corsemeier, U., Khodayar, S., Lambert, D., Kopmann, A., Kunka, N., Dick, G., Ramatschi, M., Wickert, J., Kottmeier, C., 2014. KITcube - a mobile observation system for convection studies deployed during HyMeX, Meteorologische Zeitschrift, Vol. 22, N° 6, 633-647.

Kasemir, H. W., 1960. A contribution to the electrostatic theory of lightning discharge. J. Geosphys. Res., 65, 1873-1878.

Khodayar, S., Kalthoff, N., Wickert, J., Corsmeier, U., Morcrette, C.J., Kottmeier, C., 2010. The increase of spatial data resolution for the detection of the initiation of convection. A case study from CSIP, Meteorol. Z., 19, 179-198.

Khodayar, S., Kalthoff, N., Wickert, J., Kottmeier, C., Dorninger, M., 2013. High-resolution representation of the mechanisms responsible for the initiation of isolated thunderstorms over flat and complex terrains: Analysis of CSIP and COPS cases, Meteor. Atmos. Phys., 119, 109-124.

Koshak, W. J., Solakiewicz, R. J., Blakeslee, R. J., Goodman, S. J., Christian, H. J., Hall, J. M., Bailey, J. C., Krider, E. P., Bateman, M. G., Boccippio, D. J., Mach, D. M., McCaul, E. W., Stewart, M. F., Buechler, D. E., Petersen, W. A., Cecil, D. J., 2004. North Alabama Lightning Mapping Array (LMA): VHF source retrieval algorithm and error analyses. Journal of Atmospheric and Oceanic Technology, 21(4), 543–558. https://doi.org/10.1175/1520-0426(2004)021<0543:NALMAL>2.0.CO;2.

Kotroni, V., Lagouvardos, K., 2016. Lightning in the Mediterranean and its relation with sea-surface temperature. Environ. Res. Lett. 11, 034006. https://doi.org/10.1088/1748-9326/11/3/034006.

Kottmeier, C., Palacio-Sese, P., Kalthoff, N., Corsmeier, U., Fiedler, F., 2000. Sea breezes and coastal jets in southeastern Spain, Int. J. Climatol., 20, 1791–1808.

Lagouvardos, K., Dafis, S., Giannaros, C., Karagiannidis, A., and Kotroni, V., 2020. Investigating the role of extreme synoptic patterns and complex topography during two heavy rainfall events in Crete in February 2019, Climate, 8, 87, doi:10.3390/cli8070087.

Lambert, D., Mallet, M., Ducrocq, V., Dulac, F., Gheusi, F., Kalthoff, N., 2011. CORSiCA: a Mediterranean atmospheric and oceanographic observatory in Corsica within the framework of HyMeX and ChArMEx, Adv. Geosci., 26, 125-131.

Lang, T. J., Miller, L. J., Weisman, M., Rutledge, S. A., Barker, L. J., Bringi, V. N., Chandrasekar, V., Detwiler, A., Doesken, N., Helsdon, J., Knight, C., Krehbiel, P., Lyons, W. A., MacGorman, D., Rasmussen, E., Rison, W., Rust, W. D., Thomas, R. J., 2004. The severe thunderstorm electrification and precipitation study, Bull. Am. Meteorol. Soc., 85(8), 1107-1125, doi.org/10.1175/BAMS-85-8-1107.

Lang, T. J., Rutledge, S. A., 2011. A framework for the statistical analysis of large radar and lightning datasets: Results from steps 2000, Mon. Wea. Rev., 139(8), 2536–2551, doi.org/10.1175/MWR-D-10-05000.1.

Lang, T. J., Ávila, E. E., Blakeslee, R. J., Burchfield, J., Wingo, M., Bitzer, P. M., Carey, L. D., Deierling, W., Goodman, S. J., Medina, B. L., Melo, G., Pereyra, R. G., 2020. The relampago lightning mapping array: Overview and initial comparison with the geostationary lightning mapper, J. Atmos. Ocean. Tech., 37(8), 1457–1475, doi.org/10.1175/JTECH-D-20-0005.1.

Li, Y., Zhang, G., Wang, Y., Wu, B., Li, J., 2017. Observation and analysis of electrical structure change and diversity in thunderstorms on the Qinghai-Tibet Plateau, Atmos. Res., 194, 130–141, doi.org/10.1016/j.atmosres.2017.04.031.

López, J. A., Montanyà, J., van der Velde, O. A., Pineda, N., Salvador, A., Romero, D., Aranguren, D., Taborda, J., 2019. Charge Structure of Two Tropical Thunderstorms in Colombia, J. Geophys. Res. Atmospheres, 124(10), 5503-5515, doi.org/10.1029/2018JD029188.

MacGorman, D. R., Rust, W. D., Krehbiel, P. R., Rison, W., Bruning, E. C., Wiens, K., 2005. The electrical structure of two supercell storms during STEPS, Mon. Weather Rev., 133, 2583–2607.

MacGorman, D. R., Rust, W. D., Schuur, T. J., Biggerstaff, M. I., Straka, J. M., Ziegler, C. L., Mansell, E. R., Bruning, E. C., Kuhlman, K. M., Lund, N. R., Biermann, N. S., Payne, C., Carey, L. D., Krehbiel, P. R., Rison, W., Eack, K. B., Beasley, W. H., 2008. TELEX: The Thunderstorm Electrification and Lightning Experiment, Bull. Am. Meteorol. Soc., 89, 997–1013.

Mansell, E. R., 2005. Charge structure and lightning sensitivity in a simulated multicell thunderstorm, J. Geophys. Res., 110, D12101, doi.org/10.1029/2004JD005287.

Mansell, E. R., Ziegler, C. L., Bruning, E .C., 2010. Simulated electrification of a small thunderstorm with two-moment bulk microphysics, J. Atmos. Sci., 67, 171-194.

Metzger, J., Barthlott, C., Kalthoff, N., 2014. Impact of upstream flow conditions on the initiation of moist convection over the island of Corsica, Atmos. Res., 145–146, 279–296, doi.org/10.1016/j.atmosres.2014.04.011.

Myhre, G., Myhre, C. E. L., Samset, B. H. Storelvmo, T., 2013. Aerosols and their Relation to Global Climate and Climate Sensitivity. Nature Education Knowledge 4(5):7.

Pereyra, R. G., Avila, E. E., Castellano, N. E., Saunders, C. P. R., 2000. A laboratory study of graupel charging. J. Geophys. Res. 105, 20803–20813.

Poelman, D.R., Schulz, W., Diendorfer, G., Bernardi, M., 2016. The European lightning location system EUCLID – part 2: observations. Nat. Hazards Earth Syst. Sci. 16, 607–616. https://doi.org/10.5194/nhess-16-607-2016.

Qian, J.-H., 2007. Why precipitation is mostly concentrated over islands in the maritime continent, J. Atmos. Sci. 65, 1428-1441.

Qie, X., Zhang, T., Chen, C., Zhang, G., Zhang, T., Wei, W., 2005. The lower positive charge center and its effect on lightning discharges on the Tibetan Plateau, Geophys. Res. Lett., 32(5), 1–4, https://doi.org/10.1029/2004GL022162.

Ribaud, J.-F., Bousquet, O., Coquillat, S., 2016. Relationships between total lightning activity, microphysics and kinematics during the 24 September 2012 HyMeX bow-echo system, Q. J. R. Meteorol. Soc. 142 (Suppl 1): 298–309, August 2016 DOI:10.1002/qj.2756.

Ricard, D., Ducrocq, V., Auger, L., 2012. A Climatology of the Mesoscale Environment Associated with Heavily Precipitating Events over a Northwestern Mediterranean Area, J. Appl. Meteorol. Clim., 51, 468–488, doi.org/10.1175/jamc-d-11-017.1.

Rienecker, M.M., M.J. Suarez, R. Todling, J. Bacmeister, L. Takacs, H.-C. Liu, W. Gu, M. Sienkiewicz, R.D. Koster, R. Gelaro, I. Stajner, and J.E. Nielsen, 2008. The GEOS-5 Data Assimilation System - Documentation of Versions 5.0.1, 5.1.0, and 5.2.0. Technical Report Series on Global Modeling and Data Assimilation, 27.

Rosenfeld, D., Lohmann, U., Raga, G. B., O'Dowd, C. D., Kulmala, M., Fuzzi, S., Reissell, A., Andreae, M. O., 2008. Flood or drought: how do aerosols affect precipitation? Science, 321, 1309-1313, DOI: 10.1126/science.1160606.

Rust, W. D., MacGorman, D. R., Bruning, E. C., Weiss, S. A., Krehbiel, P. R., Thomas, R. J., Rison, W., Hamlin, T., Harlin, J., 2005. Inverted-polarity electrical structures in thunderstorms in the Severe Thunderstorm Electrification and Precipitation Study (STEPS), Atmos. Res., 76(1–4), 247–271, doi.org/10.1016/j.atmosres.2004.11.029.

Salvador, A., Pineda, N., Montanyà, J., López, J. A., Solà, G., 2021. Thunderstorm charge structures favouring cloud-to-ground lightning, Atmos. Res., 257(March), 105577, doi.org/10.1016/j.atmosres.2021.105577.

Saunders, C. P. R., 2008. Charge separation mechanisms in clouds, Space Sci. Rev., 137, 335-353, doi.org/10.1007/s11214-008-9345-0.

Saunders, C. P. R., Peck, S.L., 1998. Laboratory studies of the influence of the rime accretion rate on charge transfer during crystal/graupel collisions, J. Geophys. Res., 103, 13,949-13,956.

Scheffknecht, P., Richard, E., Lambert, D., 2016. A Highly Localized High Precipitation Event over Corsica, Quart. J. Roy. Meteor. Soc., Special issue "Advances in understanding and forecasting of heavy precipitation in the Mediterranean through the HyMeX SOP1 field campaign", Volume 142, Issue S1, August 2016, pp 206-221, DOI:10.1002/qj.2795.

Scheffknecht, P., Richard, E., Lambert, D., 2017. Climatology of heavy precipitation over Corsica in the period 1985–2015, Quart. J. Roy. Meteor. Soc., 143: 2987-2998, DOI:10.1002/qj.3140.

Seity, Y., Brousseau, P., Malardel, S., Hello, G., Bénard, P., Bouttier, F., Masson, V., 2011. The AROME-France convective-scale operational model. Monthly Weather Review, 139(3), 976-991.

Soriano, L. R., de Pablo, F., Tomas, C., 2019. Ten-year study of cloud-to-ground lightning activity in the Iberian Peninsula. J. of Atmospheric and Solar-Terrestrial Physics, 67, 1632–1639. https://doi.org/10.1016/j.jastp.2005.08.019.

Stein, A.F., Draxler, R.R, Rolph, G.D., Stunder, B.J.B., Cohen, M.D., Ngan, F., 2015. NOAA's HYSPLIT atmospheric transport and dispersion modeling system, Bull. Amer. Meteor. Soc., 96, 2059-2077, http://dx.doi.org/10.1175/BAMS-D-14-00110.1.

Stolzenburg, M., Rust, W. D., Marshall, T. C., 1998. Electrical structure in thunderstorm convective regions 3. Synthesis, J. Geophys. Res., 103, 14097-14108.

Stough, S. M., & Carey, L. D., 2020. Observations of anomalous charge structures in supercell thunderstorms in the Southeastern United States. J. Geophys. Res. Atmospheres, 125(17), e2020JD033012. https://doi.org/10.1029/2020jd033012.

Stough, S. M., Carey, L. D., Schultz, C. J., & Cecil, D. J., 2021. Examining conditions supporting the development of anomalous charge structures in supercell thunderstorms in the Southeastern United States. Journal of Geophysical Research: Atmospheres, 126(16), 1–31. https://doi.org/10.1029/2021JD034582.

Takahashi, T., 1978. Riming electrification as a charge generation mechanism in thunderstorms, J. Atmos. Sc., 35, 1536-1548, doi.org/10.1175/1520-0469(1978)035<1536:REAACG>2.0.CO;2.

Taszarek, M., Allen, J., Pučik, T., Groenemeijer, P., Czernecki, B., Kolendowicz, L., Lagouvardos, K., Kotroni, V., Schulz, W., 2019. A climatology of thunderstorms across Europe from a synthesis of multiple data sources. J. Clim. 32, 1813–1837. https://doi.org/10.1175/JCLI-D-18-0372.1.

Taylor, C., Parker, D., Kalthoff, N., Gaertner, M. A., Philippon, N., Bastin, S., Harris, P. P., Boone, A., Guichard, F., Agusti-Panareda, A., Baldi, M., Cerlini, P., Descroix, L., Douville, H., Flamant, C., Grandpeix, J.-Y., Polcher, J., 2011. New perspectives on land-atmosphere feedbacks from the African monsoon multidisciplinary analysis, Atmos. Sci. Lett., 12, 38-44.

Tessendorf, S. A., Miller, L. J., Wiens, K. C., Rutledge, S.A., 2005. The 29 June 2000 supercell observed during STEPS. Part I: Kinematics and micro- physics, J. Atmos. Sci., 62, 4127-4150.

Tessendorf, S. A., Rutledge, S. A., Wiens, K. C., 2007. Radar and lightning observations of normal and inverted polarity multicellular storms from STEPS, Mon. Weather Rev. 135.

Thomas, R. J., Krehbiel, P. R., Rison, W., Hamlin, T., Harlin, J., Shown, D., 2001. Observations of VHF source powers radiated by lightning, Geophys. Res. Lett., Vol. 28, No. 1, 143-146, January 1.

Thomas, R. J., Krehbiel, P. R., Rison, W., Harlin, J., Hamlin, T., Campbell, N., 2003. The LMA flash algorithm, Proceedings of the 12th International Conference on Atmospheric Electricity, 489-492, Versailles, 9-12 June.

Thomas, R. J., Krehbiel, P. R., Rison, W., Hunyady, S. J., Winn, W. P., Hamlin, T., Harlin, J., 2004. Accuracy of the Lightning Mapping Array, J. Geophys. Res., 109, D14207, doi.org/10.1029/2004JD004549.

Tidiga, M., S. Coquillat, D. Ricard, E. Defer, P. De Guibert, D. Lambert, J.-P. Pinty, V. Pont, S. Prieur, 2018. Daytime convection in Corsica in absence of synoptic forcing: fine-scale analysis of the relief and coastal breezes influence using lightning observation (SAETTA) and high-resolution numerical simulation (Meso-NH), 11th HyMeX Workshop, 29 May-2 June, Lecce, Italy.

Weckwerth, T.M., 2000. The effect of small-scale moisture variability on thunderstorm initiation, Mon. Wea. Rev., 128, 4017-4030.

Wiens, K. C., Rutledge, S. A., Tessendorf, S. A., 2005. The 29 June 2000 supercell observed during STEPS. Part II: Lightning and charge structure, J. Atmos. Sci., 62, 4151-4177.

Williams, E. R., 1989. The Tripole Structure of Thunderstorms. J. Geophys. Res., 94, 13151-13167.

Williams, E., Chan, T., Boccippio, D., 2004. Islands as miniature continents: another look at the land-continent lightning contrast, J. Geophys. Res., 109, D16206, doi:10.1029/2003JD003833.

Williams, E. R., 2006. Problems in lightning physics - the role of polarity asymmetry, Plasma Sources Sci. Technol., 15, S91–S108, doi:10.1088/0963-0252/15/2/S12.

Wilson, J. W., Carbone, R. E., Tuttle, J. D., Keenan, T. D., 2001. Tropical island convection in the absence of significant topography: Part II: Nowcasting storm evolution, Mon. Wea. Rev., 129, 1637-1655.

Zheng, D., Wang, D., Zhang, Y., Wu, T., Takagi, N., 2019. Charge Regions Indicated by LMA Lightning Flashes in Hokuriku's Winter Thunderstorms, J. geophys. Res. Atmospheres, 124(13), 7179-7206, doi.org/10.1029/2018JD030060.

Figure captions

Figure 1: Updraft core charge distribution (red + and blue -) and approximate vertical distribution of the number of VHF sources (green line) for normal and anomalous charge structures (adapted from Fusch et al., 2015): (a) normal tripole, (b) inverted tripole, (c) bottom heavy tripole, (d) negative dipole observed in Corsica. Each dipolar substructure is indicated in red (positive dipole constituted of a positive charge region overlying a negative charge region) and blue (negative dipole constituted of a negative charge region overlying a positive charge region).

Figure 2: Number of VHF sources per km² (left side) and number of lightning days per km² (right side) in linear scale (dark blue: 0; dark red: maximum value indicated in each panel) over the 2014-2019 period. Each figure is composed of 4 panels:, (a, e) vertical projection versus longitude in the top rectangle (per 0.1 km^2), (b, f) altitude histogram in the top right small square (per 0.1 km), (c, g) horizontal projection of the distribution in the bottom left square, (d, h) vertical projection versus latitude in the bottom right rectangle (per 0.1 km^2). The position of the SAETTA stations is indicated by small green or white squares on the horizontal projections. The 1000 m altitude isocontour is displayed with a black solid line.

Figure 3: Monthly number of VHF sources per km² in log scale (top) and monthly number of lightning days per km² in linear scale (bottom) for April (left figures), May (center figures) and June (right figures) over the 2014-2019 period. Details of each figure: the same as in Figure 2 caption for each month. Maximum values corresponding to the dark red color of the color scale are indicated in each panel of each figure.

Figure 4: Monthly number of VHF sources per km² in log scale (top) and monthly number of lightning days per km² in linear scale (bottom) for July (left figures), August (center figures) and September (right figures) over the 2014-2019 period. Details of each figure: the same as in Figure 2 caption for each month. Maximum values corresponding to the dark red color of the color scale are indicated in each panel of each figure.

Figure 5: Monthly number of VHF sources per km² in log scale (top) and monthly number of lightning days per km² in linear scale (bottom) for October (left figures), November (center figures) and December (right figures) over the 2014-2019 period. Details of each figure: the same as in Figure 2 caption for each month. Maximum values corresponding to the dark red color of the color scale are indicated in each panel of each figure.

Figure 6: Inter-annual monthly number of lightning days (upper graph) over the 2014-2019 period and monthly distribution of the inter-annual average number of lightning days in terms of comparative VHF source number per lightning day (bottom graph). The number N of VHF source/day is indicated in or close to each sphere.

Figure 7: Hourly distribution of the number of lightning days per km² between 10:00 UTC and 16:00 UTC over the 2014-2019 period. (a) 10:00 – 11:00; (b) 11:00 – 12:00; (c) 12:00 – 13:00; (d) 13:00 – 14:00; (e) 14:00 – 15:00; (f) 15:00 – 16:00. Before and after this time period, the distribution exhibits only weak signals and most especially above the sea at night. The 1000 m altitude isocontour is displayed with a black or a white solid line.

Figure 8: Monthly VHF source altitude histograms for the whole 2014-2019 period, from April to August (left) and from August to December (right). The histogram for August is displayed in both figures as a reference. The orange and dashed curve corresponds to the month of October without the two major events of 14/10/2016 and 29/10/2018. The very sharp peak appearing around 9 km altitude on the October profile (see Figure 5) has been filtered out here because it is due to the signature of aircraft trajectories.

Figure 9: Ranked histogram of the number of VHF sources detected per lightning event in October from 2014 to 2019.

Figure 10: Comparative sequences of a negative dipole (10/08/2017, top) and of a normal tripole exhibiting a upper positive dipole at the same altitudes (15/10/2019, bottom) using XLMA displays of VHF sources versus time (left: (a) altitude versus time from blue at the beginning of the time sequence to red at the end of the time sequence; (b) vertical projection versus longitude; (c) altitude histogram; (d) horizontal projection; and (e) vertical projection versus latitude), and versus VHF source power (right: (f) altitude versus time; (g) vertical projection versus longitude; (h) power distribution in dBW from blue for the lowest power to red for the highest power; (i) horizontal projection; and (j) vertical projection versus latitude). XLMA software was developed by Ron Thomas (Thomas et al., 2003).

Figure 11: Aerosol Optical Thickness for dust aerosols (AOT Dust (550 nm)) and wind direction at 850 hPa, for the whole lightning event dataset over the 2014-2019 period. The red, orange and yellow spheres represent the negative dipoles. The blue, purple and green spheres represent normal tripoles. The sphere size is a proxy of the aerosol size contributing mainly to the AOT (calculated if the SDA fine mode fraction data (500 nm) from the Ersa site is available). The bigger are the spheres the coarser are the atmospheric aerosols contributing to the AOT. "ADA" stands for All Data Available (i.e. AOT Dust, Wind direction and proxy of size). "Total AOT" means that AOT stands for all types of atmospheric aerosols (data from Ersa site) as AOT Dust (dust aerosols only) was not available in the GEOS5 and CAMS databases in 2014 and 2015. "SNA" stands for Size Not Available (proxy of size not available from Ersa site - arbitrary size of spheres chosen).

Figure 12: Atmospheric aerosol (AOT Dust) versus wind direction (850 hPa) background over Corsica for every day of June 2019 (stormy days or not). See Figure 11 caption for colour and size meanings. Dark grey spheres stand for 'No Stormy' days.

Figure 13: ZT500 at 00Z the 10/06/2019 simulated by ARPEGE hydrostatic model (00 UTC array run). Altitudes of the 500 hPa layer are labeled in damgp (decameter geopotential), Temperatures in °Celsius. Wind barbs depict wind direction and force. The black rectangle materializes the SAETTA field of view.

Figure 14: MSLP (red line), and 850 hPa wet bulb potential temperature parameter (color with colorscale on the right side of the image) as simulated by the ARPEGE hydrostatic model for the 10/06/2019 at 00:00 UTC (using the 00:00 UTC run).

Figure 15: (a) MSG 10.8 IR channel the 10/06/2019 at 0:00 UTC, with colorbar in °C (b) Radar reflectivities expressed in dBz with METEORAGE discharges accumulated during 1 hour are represented using triangles (with color depending on the time).

Figure 16: Emagram corresponding to the geographical point of coordinates (42.08N, 08.65E), i.e. near Ajaccio on the central West coast of Corsica, simulated by the AROME non-hydrostatic model for the 9th of June at 22:00 UTC (using the 18:00 UTC run).

Figure 17: Backward trajectories of 6 fictive particles using the GFS NWP model. Ending point altitudes are around 2500 (red), 3200 (blue) and 4000 meters (green curves).

Figure A1: Relief map of Corsica. The regions of Cap Corse and Castagniccia and the city of Ajaccio are indicated by white arrows. All distances and altitude are in km. The origin of the reference frame corresponds to the geographical point of coordinates 42.336°N and 9.099°E.

Figure A2: SAETTA data availability calendar (in green). The months of December to March are wintering periods for the high altitude stations leading to a decrease in the sensitivity of the network.

Figure A3: Instant capture of wind map at 850 hPa and of Dust Aerosol Optical Thickness at 550 nm over the western Mediterranean basin on 14/10/2016. Green circle indicates the point of study of Corsica Island to which data in the upper left panel refer (wind direction, wind speed, and Dust AOT value). The colour bar gives the intensity of Dust AOT.

Figure A4: Instant capture of wind map at 850 hPa and Dust Aerosol Optical Thickness at 550 nm over the western Mediterranean basin on 29/10/2018. Green circle indicates the point of study of Corsica Island to which data in the upper left panel refer (wind direction, wind speed, and Dust AOT value). The colour bar gives the intensity of Dust AOT.

Table captions

Table 1: Meteorological features associated with each of the events identified in June 2019.

Table A1: Dates of the 29 anomalously electrified structures detected over the 2014-2019 period. The 8 events that occurred in June 2019 and are standing for 27.6 % of all 29 events are mentioned in bold.

1040

	Negative dipole	Z500 flux direction	MSLP (hPa)	PV1.5 anomaly	Elevated convection
June 7th	Yes	SW	1015 - flat low	No	Yes
June 8th	Yes	WSW	1020 - flat low	No	Yes
June 9th (morning)	Yes	SW	1015 - flat low	No	Yes
June 9-10th (night)	Yes	SSW	1015 - flat low	No	Yes
June 14-15th	Yes	SSW	1015 - flat low	No	Yes
June 21-22th	Yes	WSW	1015 - flat low	Yes	Yes
June 30th	No	W (through)	1015 - flat low	No	No

Table 1: Meteorological features associated with each of the events identified in June 2019.

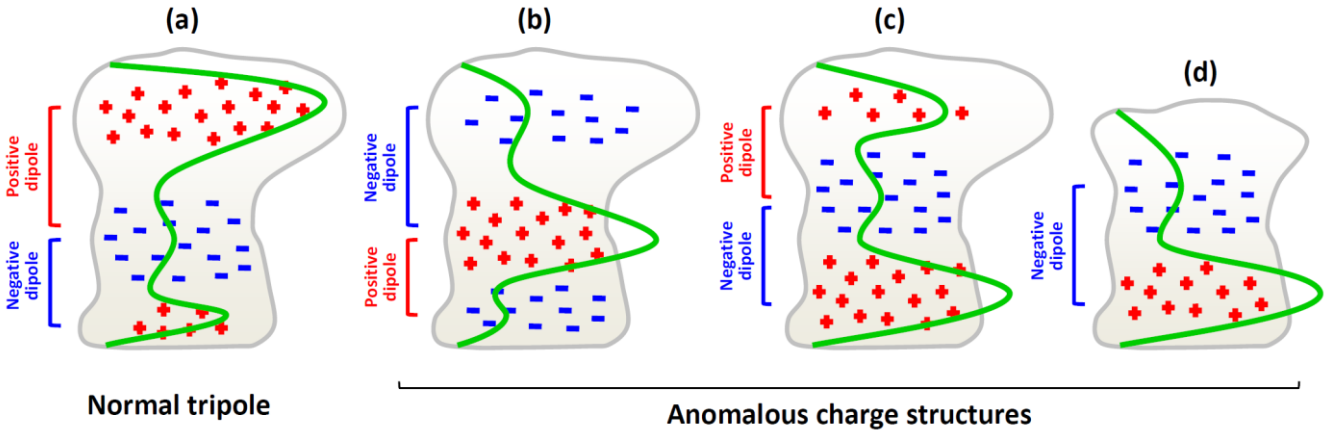

Figure 1: Updraft core charge distribution (red + and blue -) and approximate vertical distribution of the number of VHF sources (green line) for normal and anomalous charge structures (adapted from Fusch et al., 2015): (a) normal tripole, (b) inverted tripole, (c) bottom heavy tripole, (d) negative dipole observed in Corsica. Each dipolar substructure is indicated in red (positive dipole constituted of a positive charge region overlying a negative charge region) and blue (negative dipole constituted of a negative charge region overlying a positive charge region).

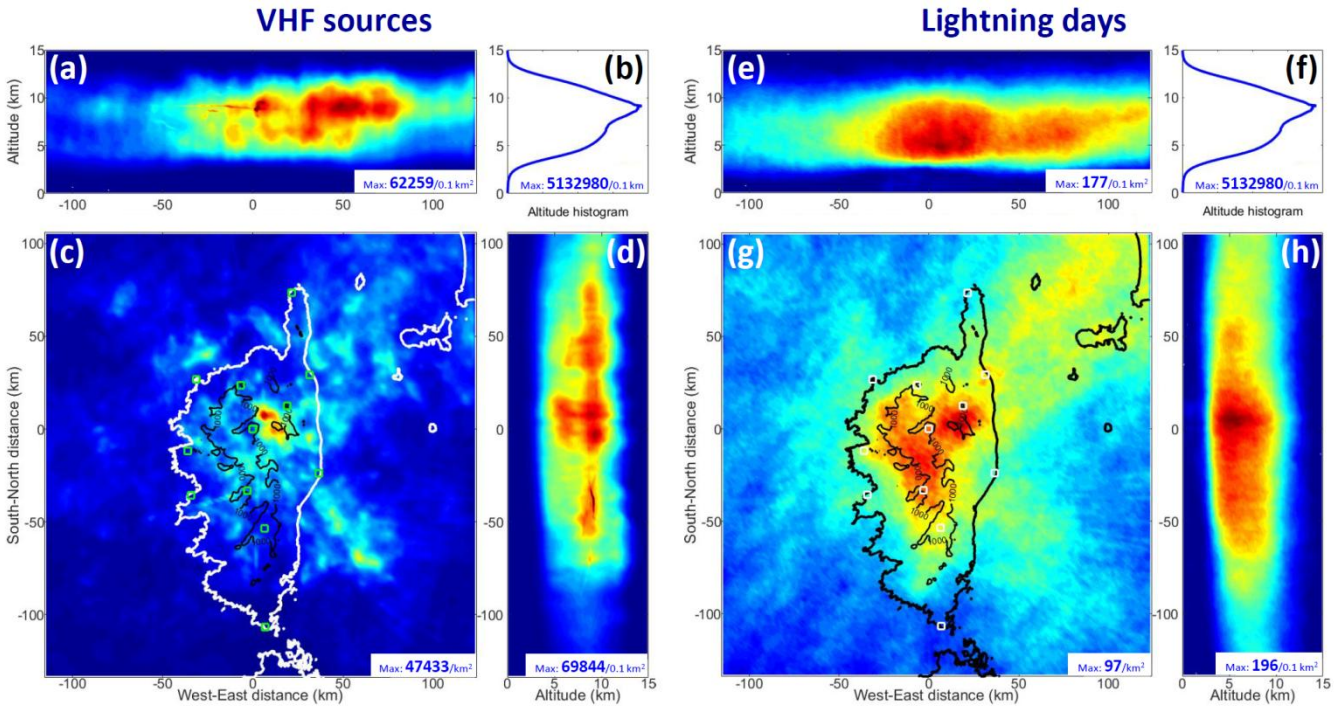

Figure 2 : Number of VHF sources per km² (left side) and number of lightning days per km² (right side) in linear scale (dark blue: 0; dark red: maximum value indicated in each panel) over the 2014-2019 period. Each figure is composed of 4 panels:, (a, e) vertical projection versus longitude in the top rectangle (per 0.1 km^2), (b, f) altitude histogram in the top right small square (per 0.1 km), (c, g) horizontal projection of the distribution in the bottom left square, (d, h) vertical projection versus latitude in the bottom right rectangle (per 0.1 km^2). The position of the SAETTA stations is indicated by small green or white squares on the horizontal projections. The 1000 m altitude isocontour is displayed with a black solid line.

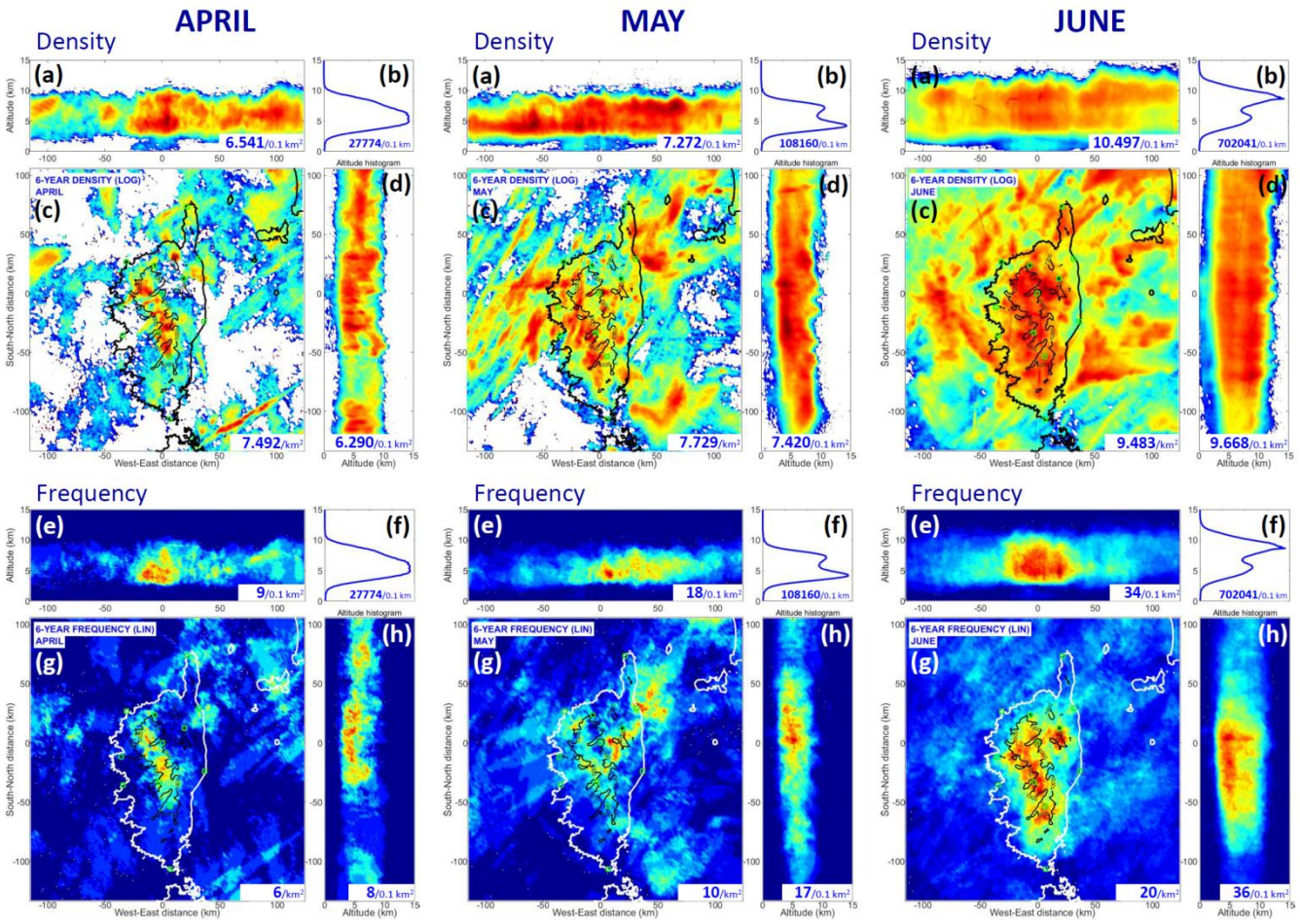

Figure 3: Monthly number of VHF sources per km² in log scale (top) and monthly number of lightning days per km² in linear scale (bottom) for April (left figures), May (center figures) and June (right figures) over the 2014-2019 period. Details of each figure: the same as in Figure 2 caption for each month. Maximum values corresponding to the dark red color of the color scale are indicated in each panel of each figure.

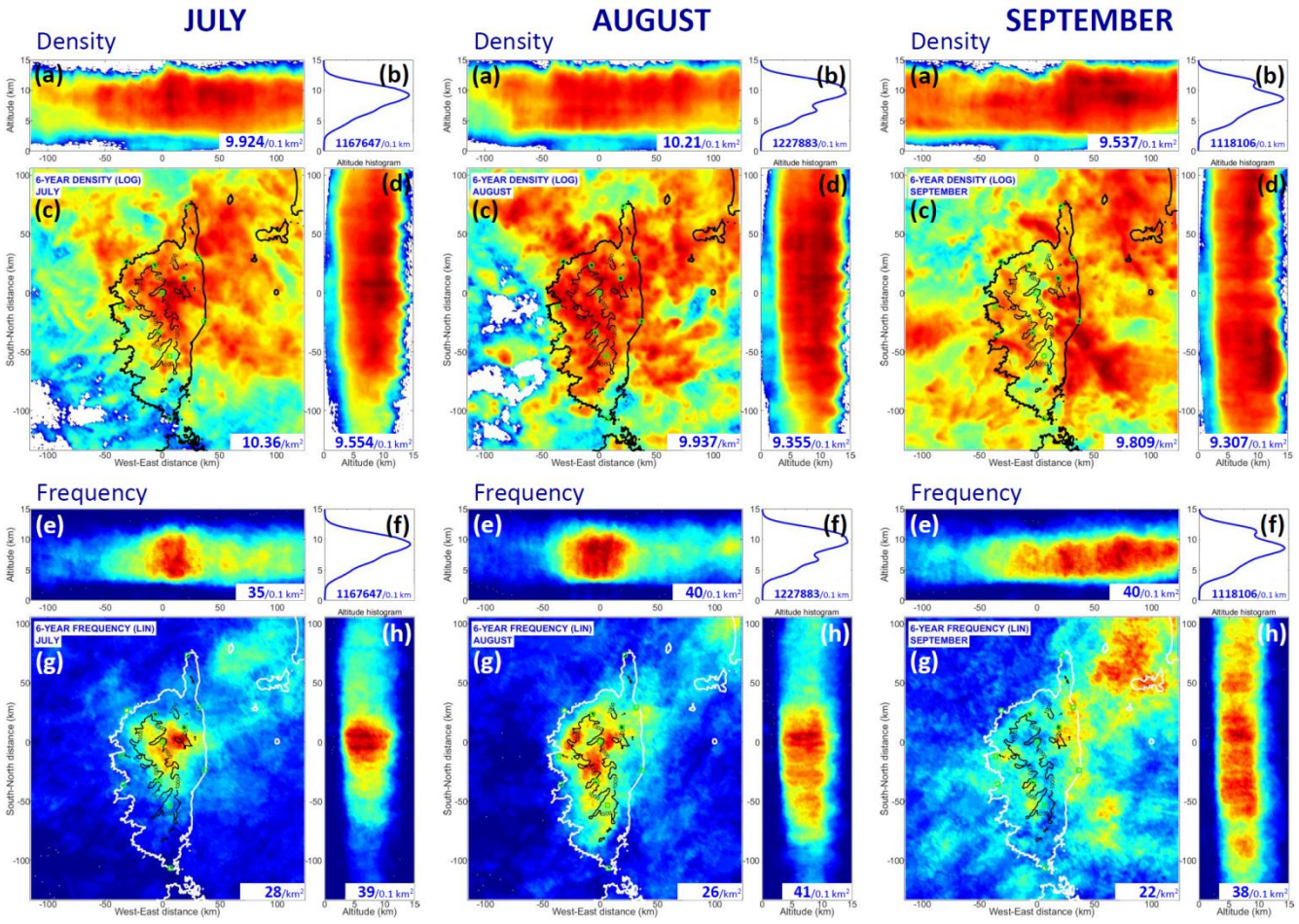

Figure 4: Monthly number of VHF sources per km² in log scale (top) and monthly number of lightning days per km² in linear scale (bottom) for July (left figures), August (center figures) and September (right figures) over the 2014-2019 period. Details of each figure: the same as in Figure 2 caption for each month. Maximum values corresponding to the dark red color of the color scale are indicated in each panel of each figure.

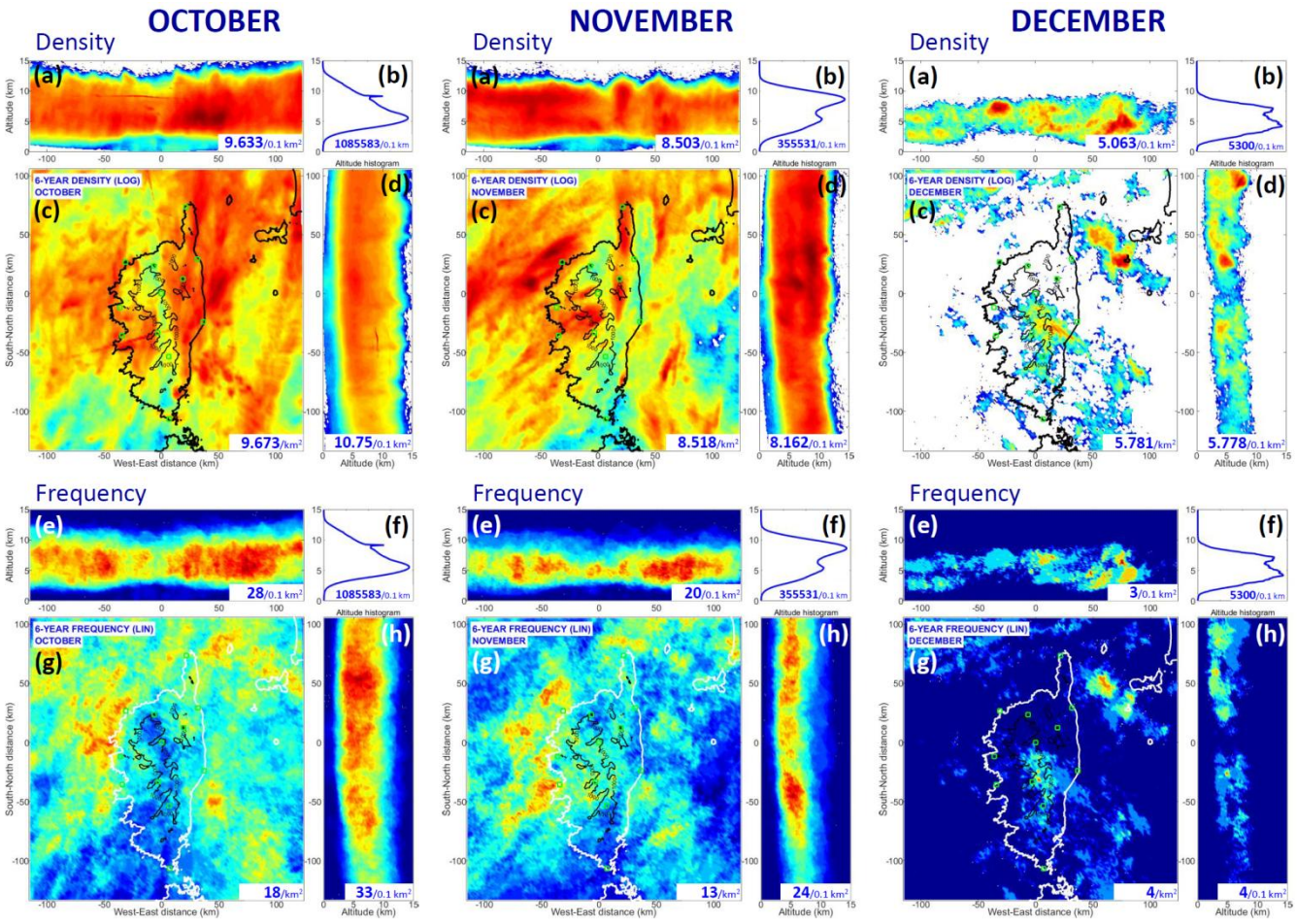

1085 **Figure 5**: Monthly number of VHF sources per km² in log scale (top) and monthly number of lightning days per km² in linear scale (bottom) for October (left figures), November (center figures) and December (right figures) over the 2014-2019 period. Details of each figure: the same as in Figure 2 caption for each month. Maximum values corresponding to the dark red color of the color scale are indicated in each panel of each figure.

1090

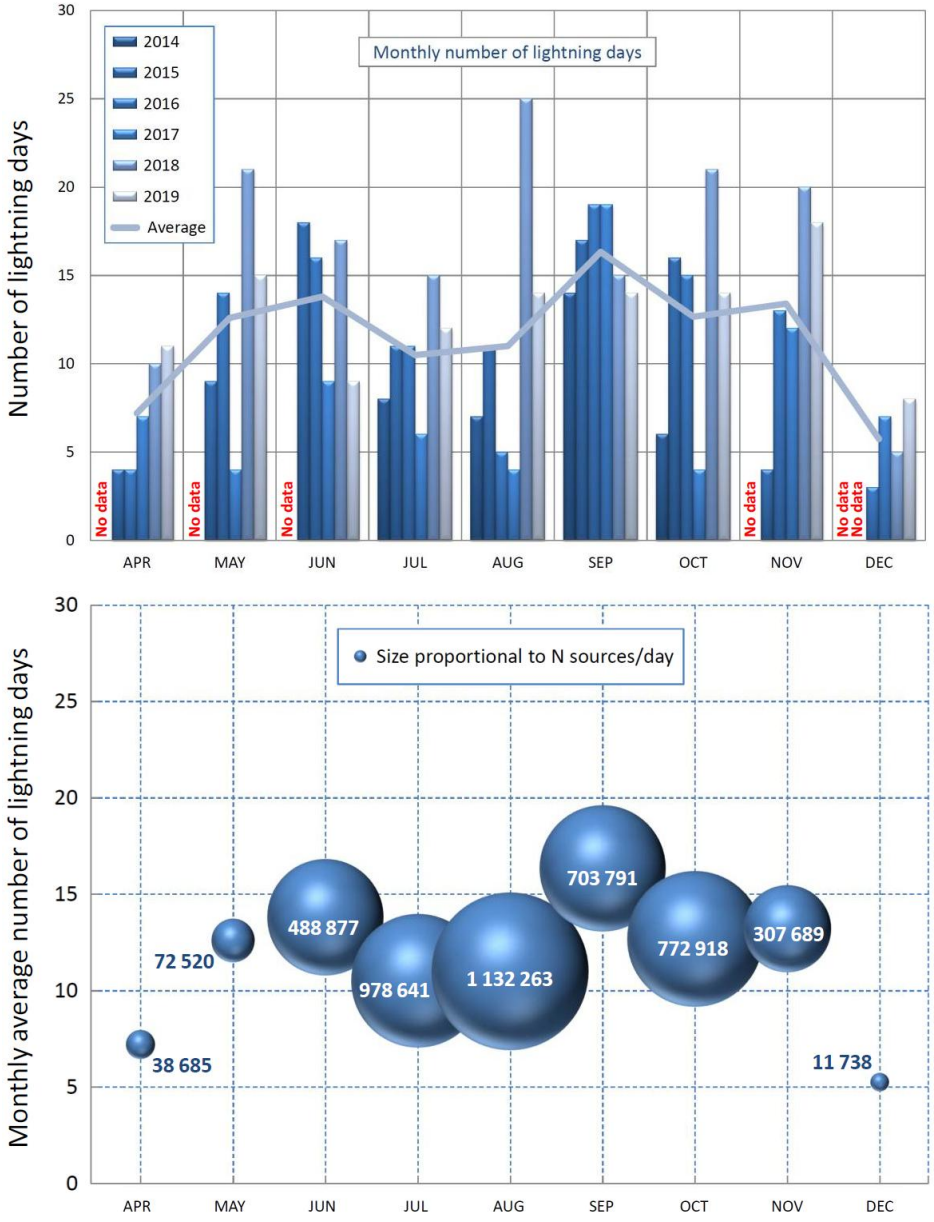

Figure 6: Inter-annual monthly number of lightning days (upper graph) over the 2014-2019 period and monthly distribution of the inter-annual average number of lightning days in terms of comparative VHF source number per lightning day (bottom graph). The number N of VHF source/day is indicated in or close to each sphere.

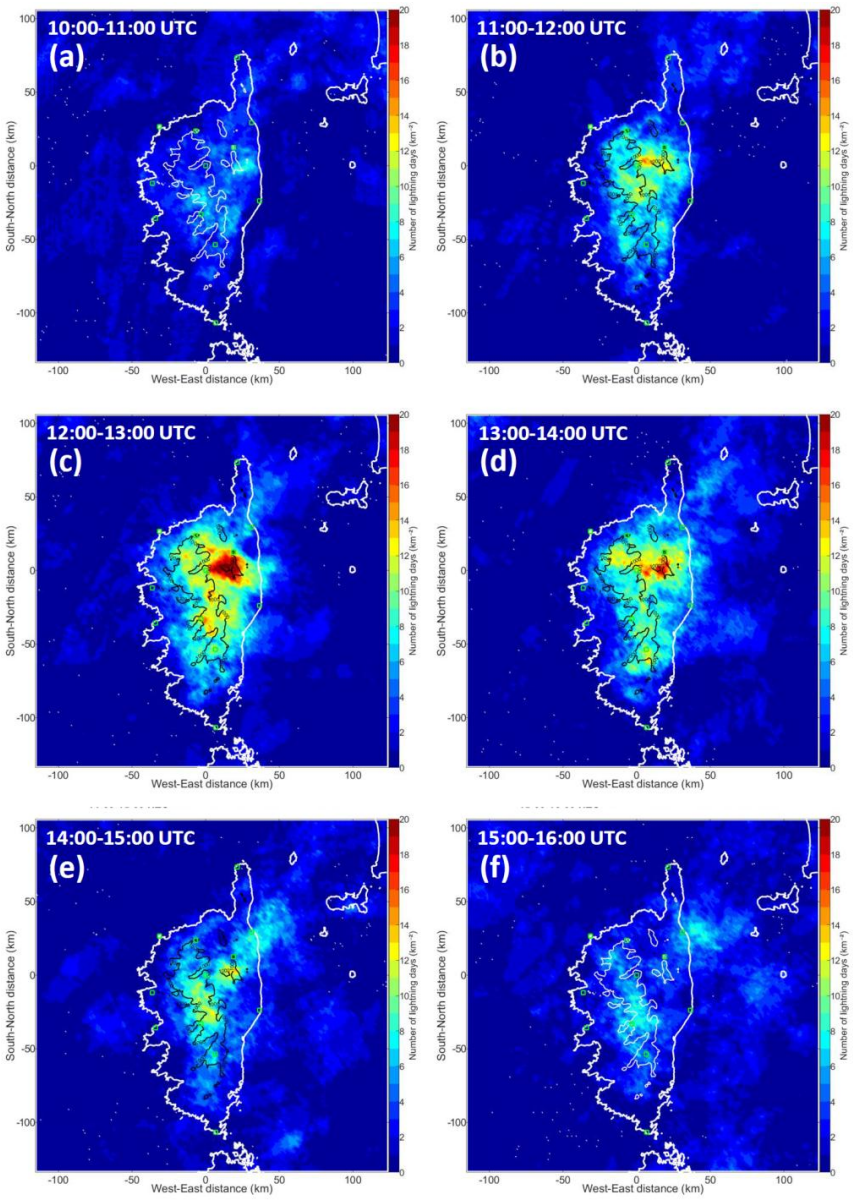

Figure 7: Hourly distribution of the number of lightning days per km² between 10:00 UTC and 16:00 UTC over the 2014-2019 period. (a) 10:00 – 11:00; (b) 11:00 – 12:00; (c) 12:00 – 13:00; (d) 13:00 – 14:00; (e) 14:00 – 15:00; (f) 15:00 – 16:00. Before and after this time period, the distribution exhibits only weak signals and most especially above the sea at night. The 1000 m altitude isocontour is displayed with a black or a white solid line.

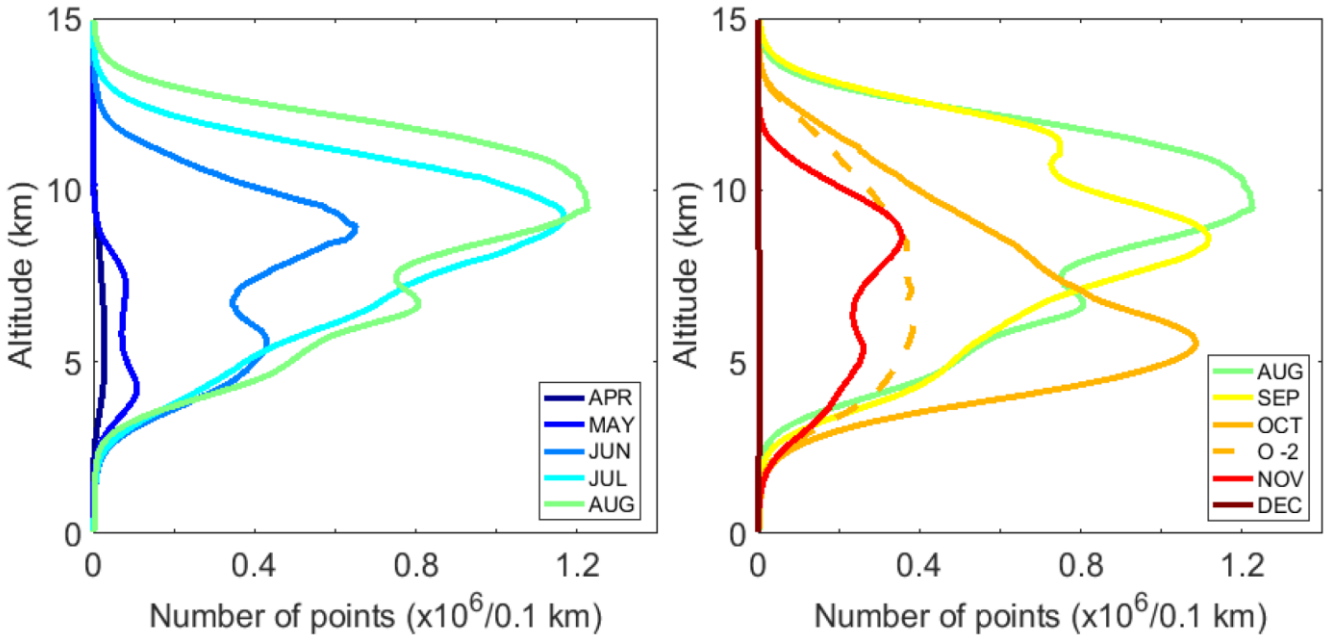

Figure 8: Monthly VHF source altitude histograms for the whole 2014-2019 period, from April to August (left) and from August to December (right). The histogram for August is displayed in both figures as a reference. The orange and dashed curve corresponds to the month of October without the two major events of 14/10/2016 and 29/10/2018. The very sharp peak appearing around 9 km altitude on the October profile (see Figure 5) has been filtered out here because it is due to the signature of aircraft trajectories.

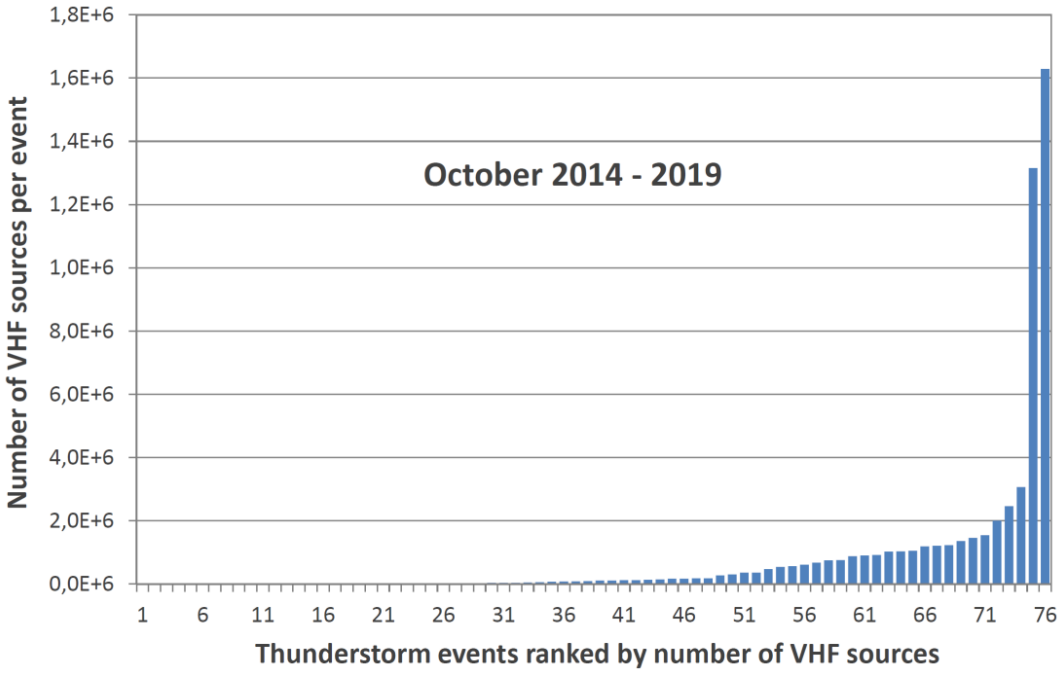

1115

Figure 9: Ranked histogram of the number of VHF sources detected per lightning event in October from 2014 to 2019.

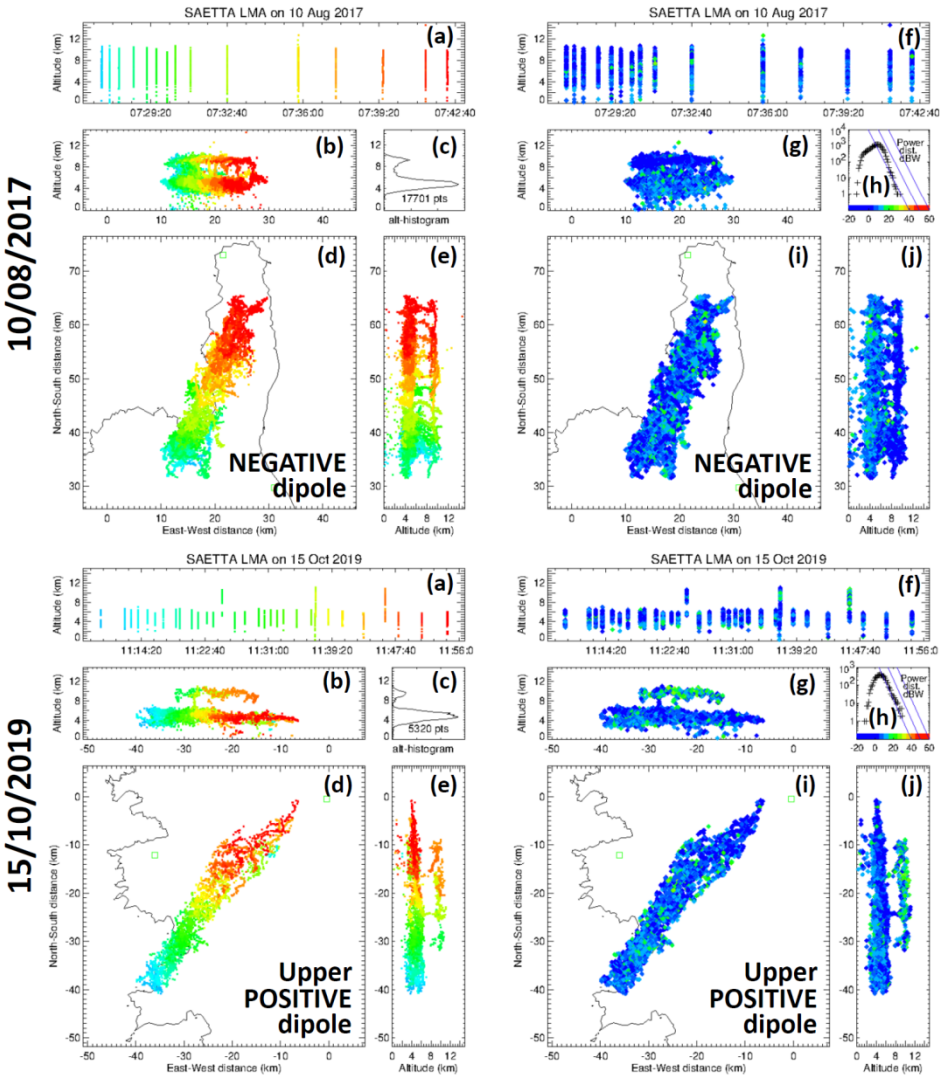

Figure 10: Comparative sequences of a negative dipole (10/08/2017, top) and of a normal tripole exhibiting a upper positive dipole at the same altitudes (15/10/2019, bottom) using XLMA displays of VHF sources versus time (left: (a) altitude versus time from blue at the beginning of the time sequence to red at the end of the time sequence; (b) vertical projection versus longitude; (c) altitude histogram; (d) horizontal projection; and (e) vertical projection versus latitude), and versus VHF source power (right: (f) altitude versus time; (g) vertical projection versus longitude; (h) power distribution in dBW from blue for the lowest power to red for the highest power; (i) horizontal projection; and (j) vertical projection versus latitude). XLMA software was developed by Ron Thomas (Thomas et al., 2003).

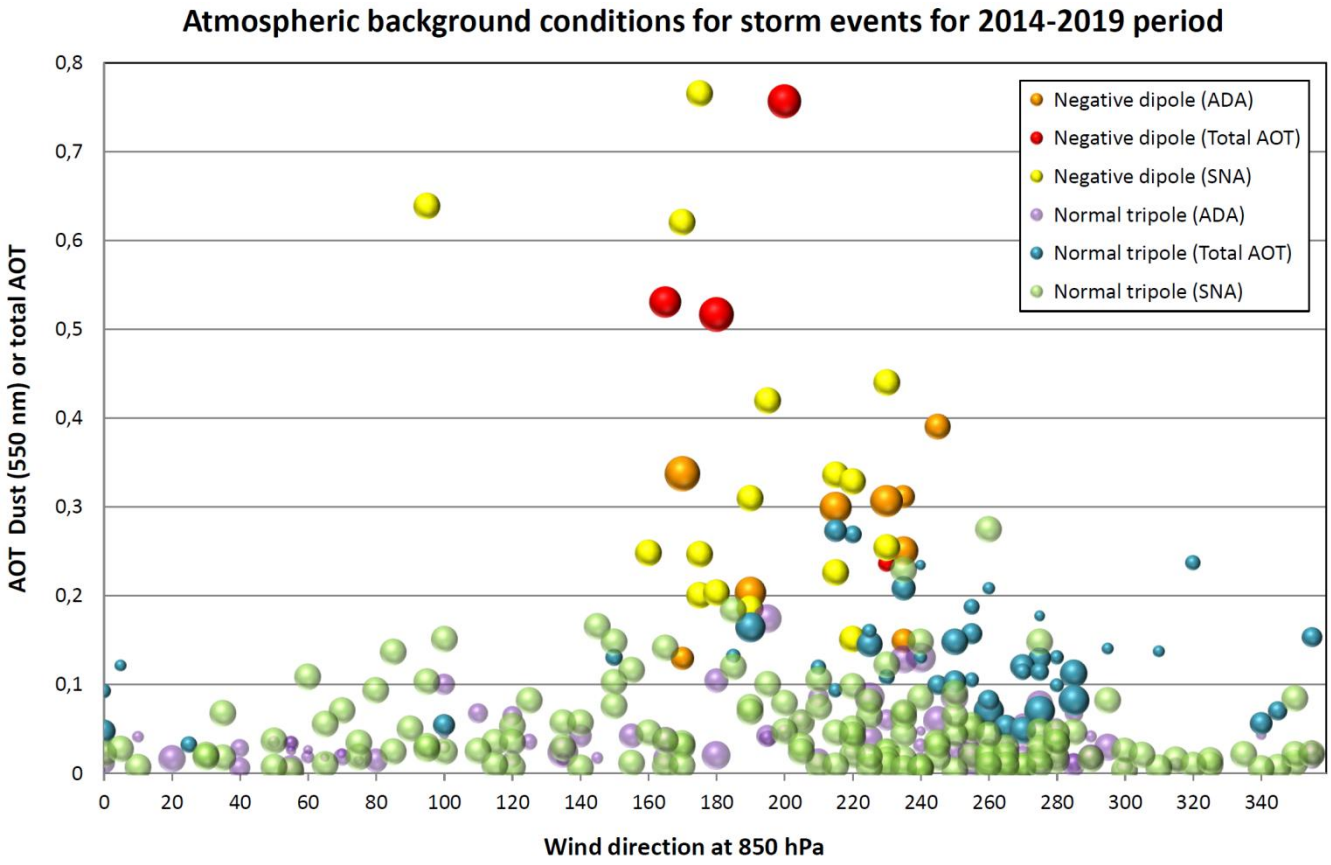

Figure 11: Aerosol Optical Thickness for dust aerosols (AOT Dust (550 nm)) and wind direction at 850 hPa, for the whole lightning event dataset over the 2014-2019 period. The red, orange and yellow spheres represent the negative dipoles. The blue, purple and green spheres represent normal tripoles. The sphere size is a proxy of the aerosol size contributing mainly to the AOT (calculated if the SDA fine mode fraction data (500 nm) from the Ersa site is available). The bigger are the spheres the coarser are the atmospheric aerosols contributing to the AOT. "ADA" stands for All Data Available (i.e. AOT Dust, Wind direction and proxy of size). "Total AOT" means that AOT stands for all types of atmospheric aerosols (data from Ersa site) as AOT Dust (dust aerosols only) was not available in the GEOS5 and CAMS databases in 2014 and 2015. "SNA" stands for Size Not Available (proxy of size not available from Ersa site - arbitrary size of spheres chosen).

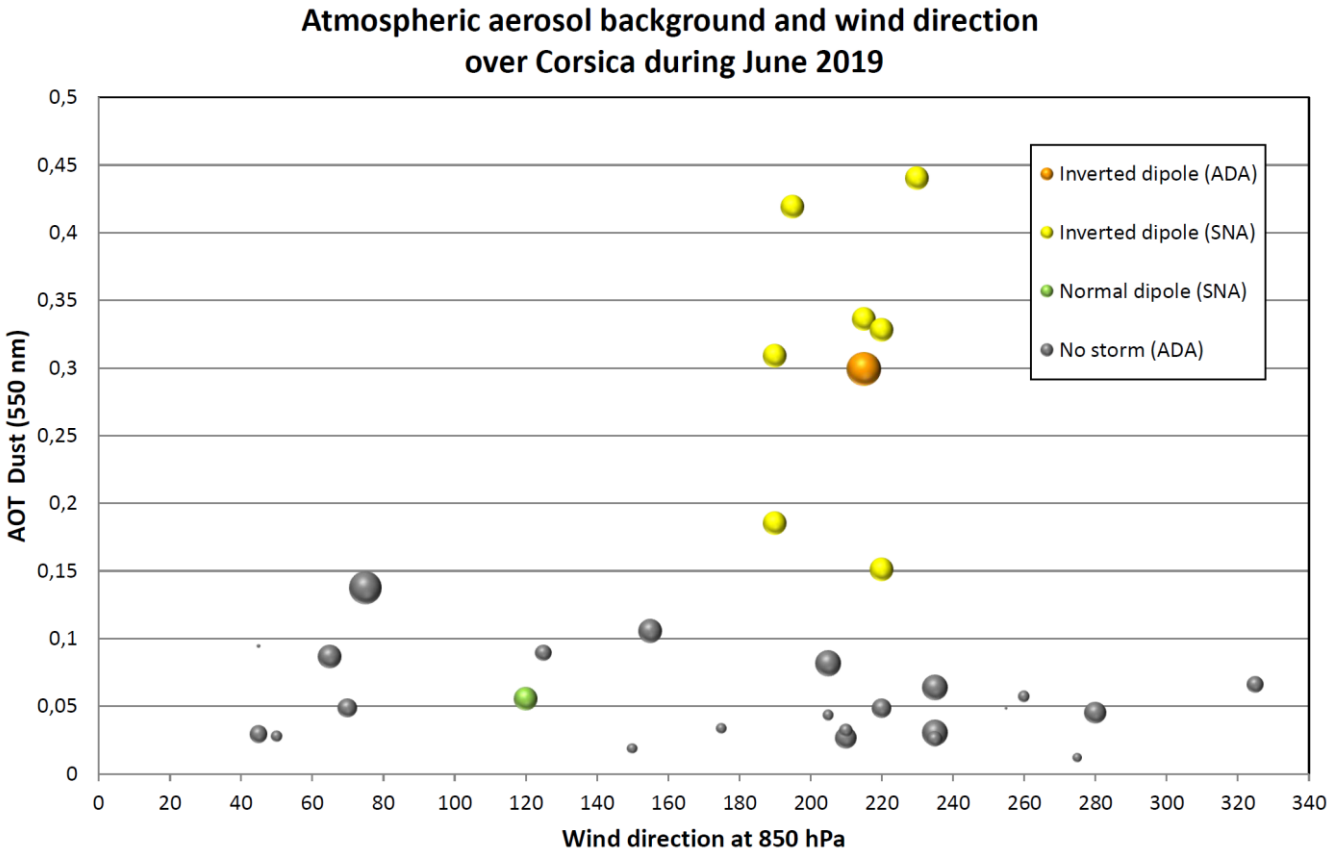

Figure 12: Atmospheric aerosol (AOT Dust) versus wind direction (850 hPa) background over Corsica for every day of June 2019 (stormy days or not). See Figure 11 caption for colour and size meanings. Dark grey spheres stand for 'No Stormy' days.

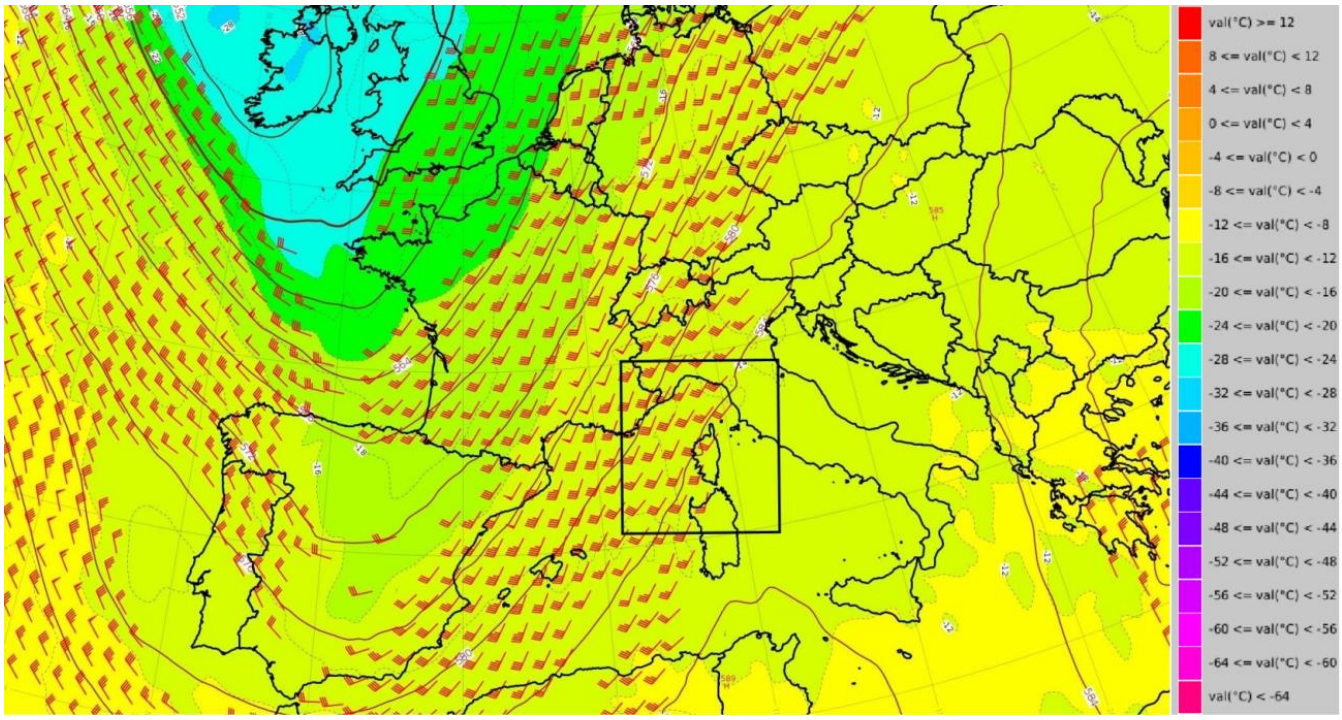

Figure 13*:* ZT500 at 00Z the 10/06/2019 simulated by ARPEGE hydrostatic model (00 UTC array run). Altitudes of the 500 hPa layer are labeled in damgp (decameter geopotential), Temperatures in °Celsius. Wind barbs depict wind direction and force. The black rectangle materializes the SAETTA field of view.

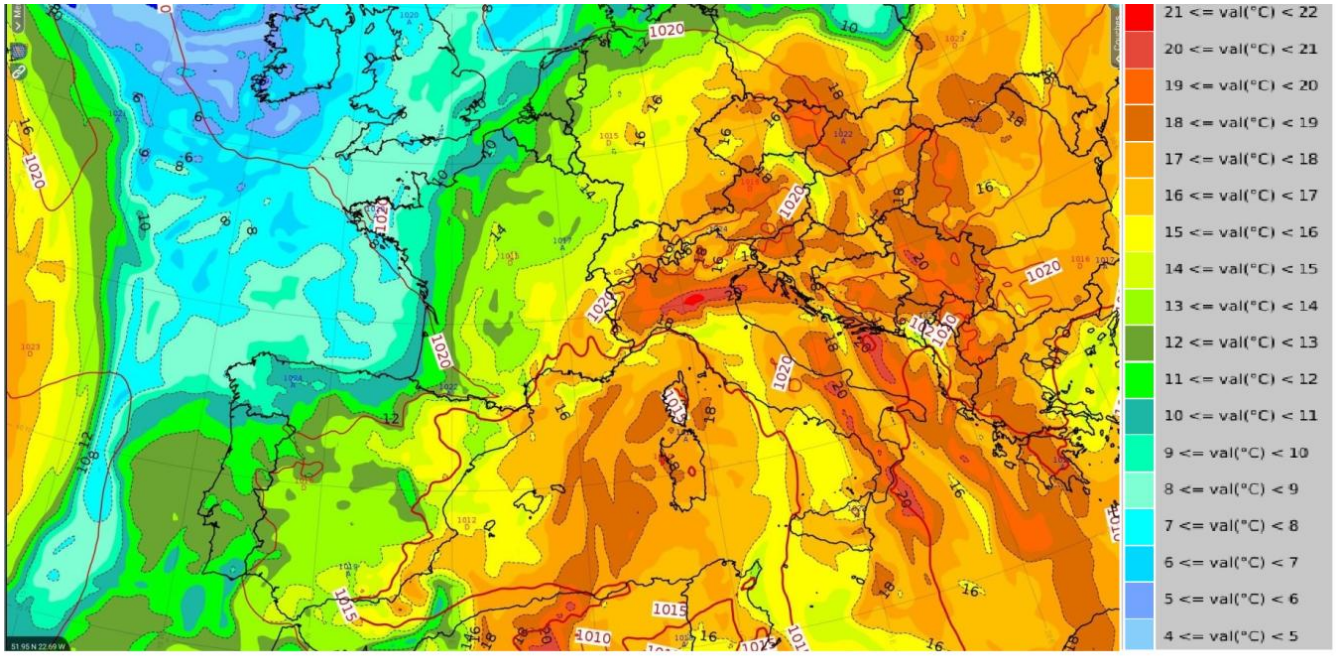

Figure 14: MSLP (red line), and 850 hPa wet bulb potential temperature parameter (color with colorscale on the right side of the image) as simulated by the ARPEGE hydrostatic model for the 10/06/2019 at 00:00 UTC (using the 00:00 UTC run)

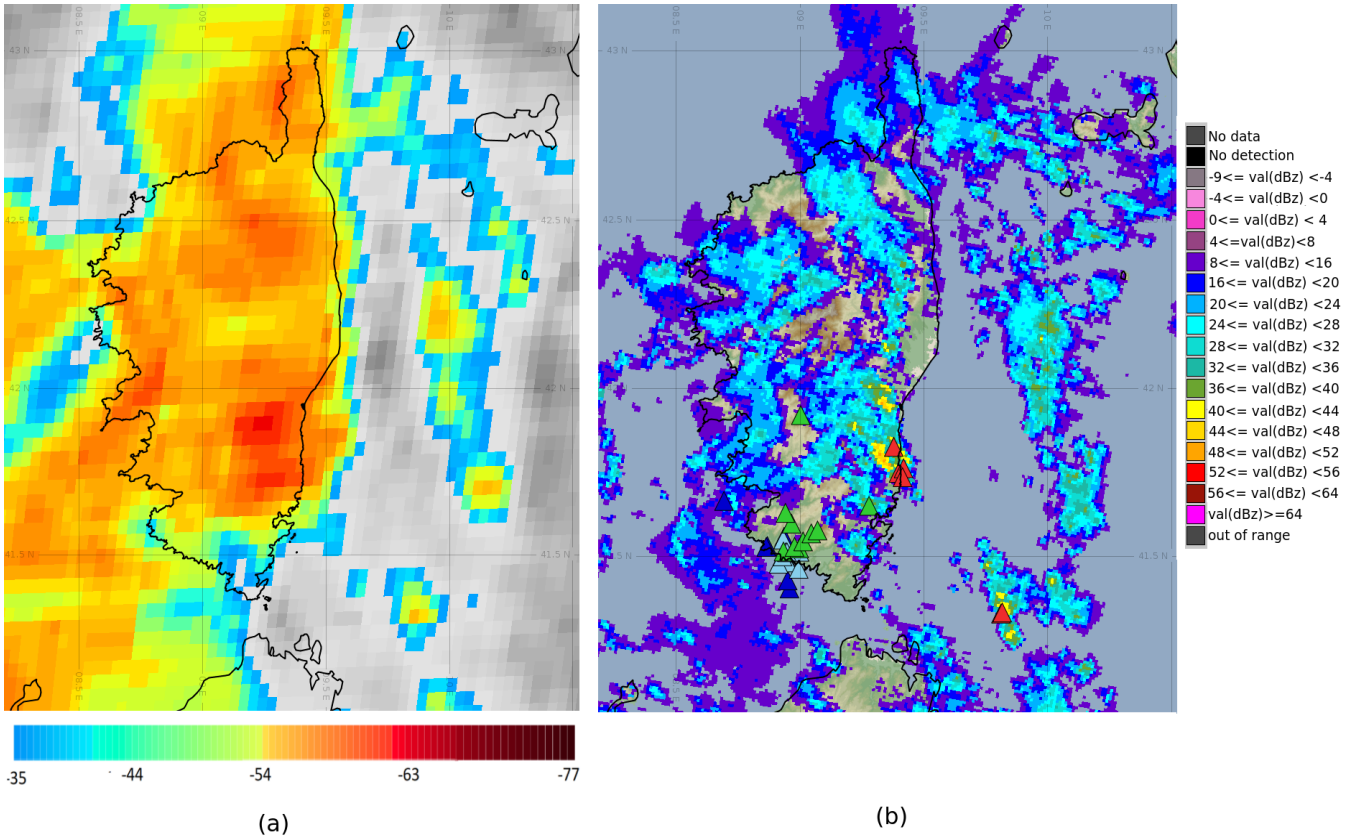

Figure 15: (a) MSG 10.8 IR channel the 10/06/2019 at 0:00 UTC, with colorbar in °C (b) Radar reflectivities expressed in dBz with METEORAGE discharges accumulated during 1 hour are represented using triangles (with colour depending on the time).

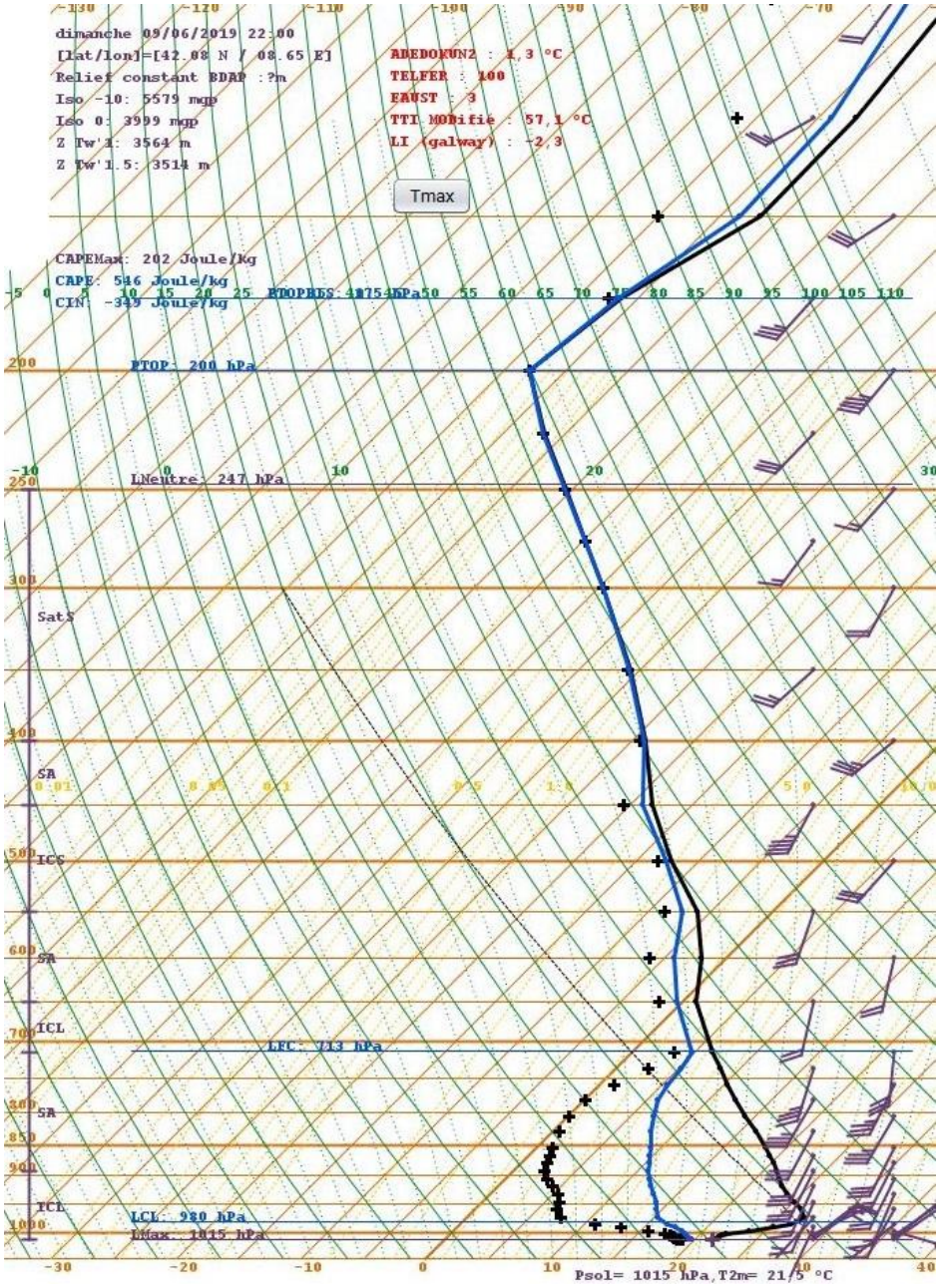

1170

Figure 16: Emagram corresponding to the geographical point of coordinates (42.08N, 08.65E), i.e. near Ajaccio on the central West coast of Corsica, simulated by the AROME non-hydrostatic model for the 9th of June at 22:00 UTC (using the 18:00 UTC run). Black line: temperature, blue line: wet bulb temperature, black crosses: dew point.

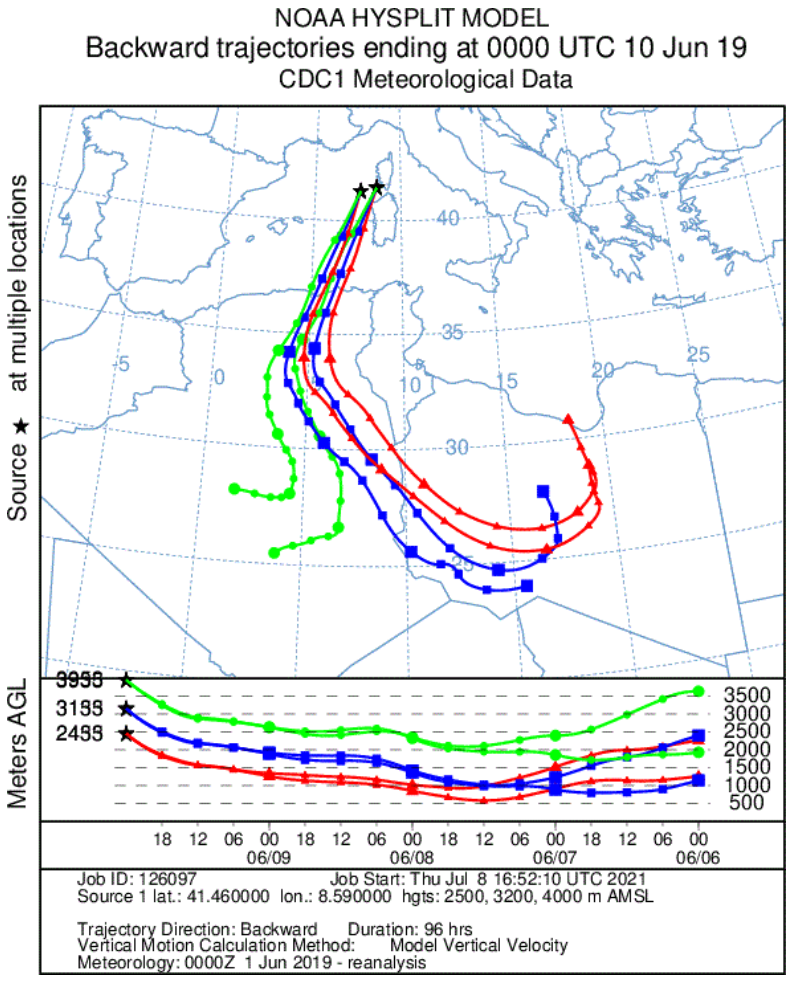

1175

Figure 17: Retro trajectories of 6 fictive particles using the GFS NWP model. Ending point altitudes are around 2500 (red), 3200 (blue) and 4000 meters (green curves).

Appendix A1: Relief map of Corsica

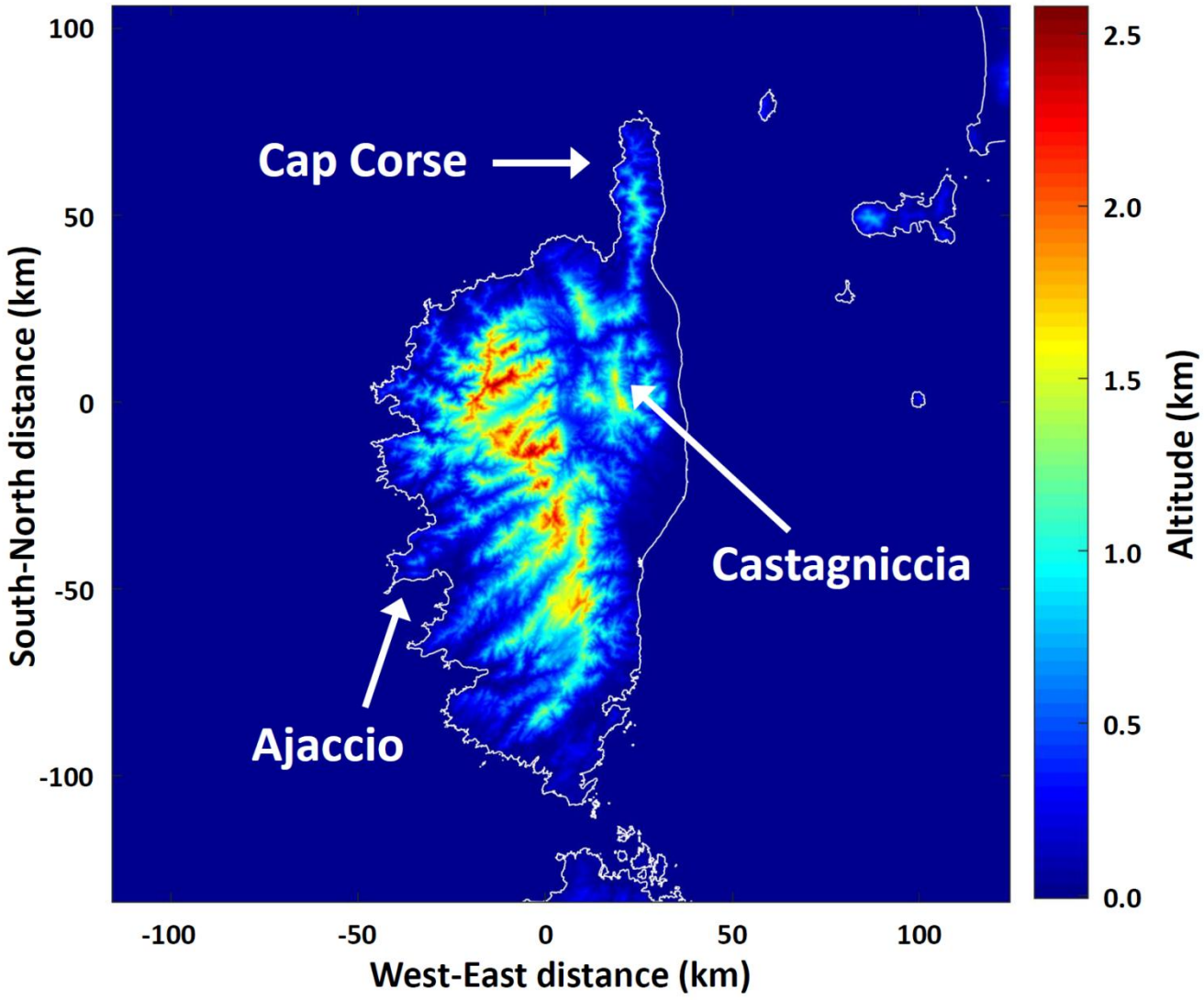

Figure A1: Relief map of Corsica. The regions of Cap Corse and Castagniccia and the city of Ajaccio are indicated by white arrows. All distances and altitude are in km. The origin of the reference frame corresponds to the geographical point of coordinates 42.336°N and 9.099°E.

Appendix A2: Table of available SAETTA data

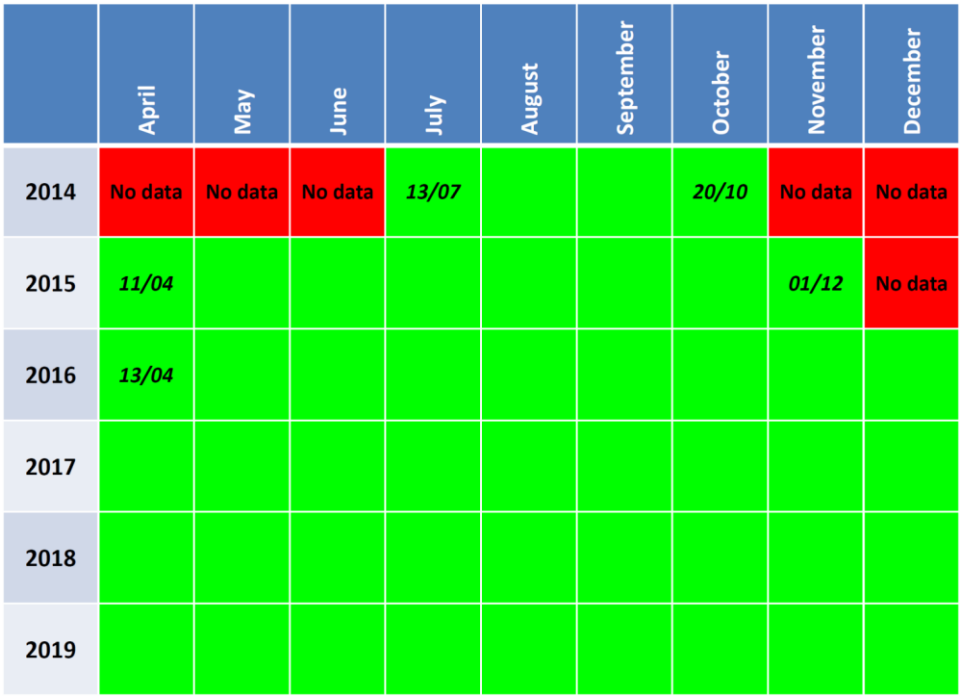

	April	May	June	July	August	September	October	November	December
2014	No data	No data	No data	*13/07*			*20/10*	No data	No data
2015	*11/04*							*01/12*	No data
2016	*13/04*								
2017									
2018									
2019									

Figure A2: SAETTA data availability calendar (in green). The months of December to March are wintering periods for the high altitude stations leading to a decrease in the sensitivity of the network.

Appendix A3: Instant capture of the aerosol and meteorological situation on 14/10/2016

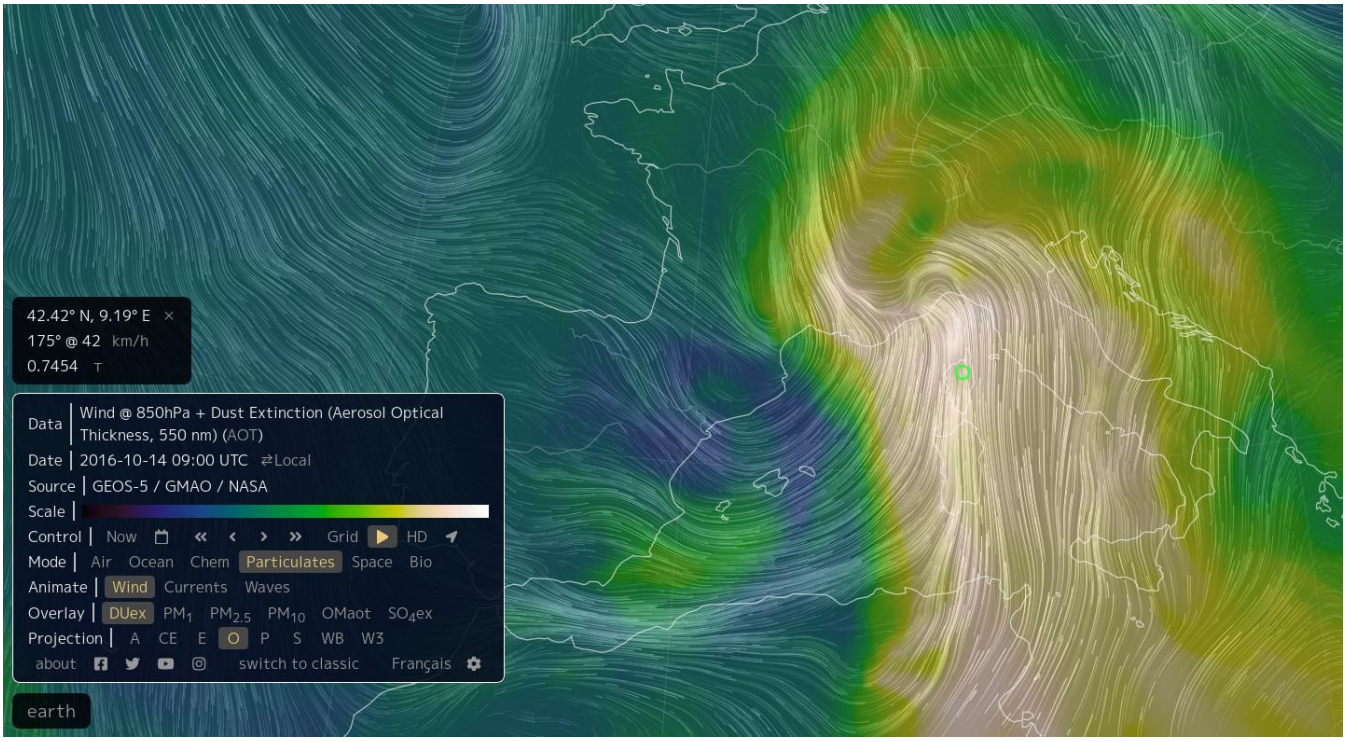

Figure A3: Instant capture of wind map at 850 hPa and of Dust Aerosol Optical Thickness at 550 nm over the western Mediterranean basin on 14/10/2016. Green circle indicates the point of study of Corsica Island to which data in the upper left panel refer (wind direction, wind speed, and Dust AOT value). The colour bar gives the intensity of Dust AOT.

Appendix A4: Instant capture of the aerosol and meteorological situation on 29/10/2018

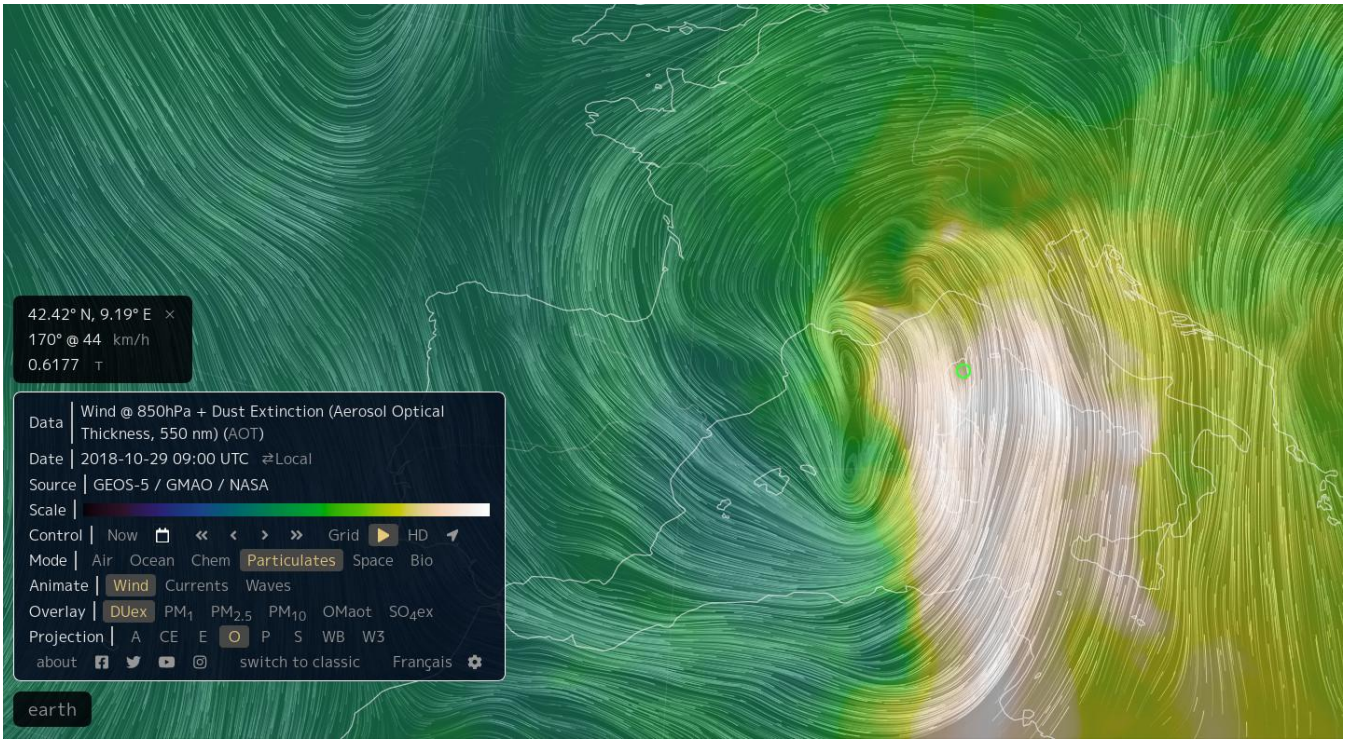

Figure A4: Instant capture of wind map at 850 hPa and Dust Aerosol Optical Thickness at 550 nm over the western Mediterranean basin on 29/10/2018. Green circle indicates the point of study of Corsica Island to which data in the upper left panel refer (wind direction, wind speed, and Dust AOT value). The colour bar gives the intensity of Dust AOT.

Appendix A5: Dates of anomalously electrified structure over the 2014-2019 period

Date of anomalously electrified structure over the 2014-2019 period
20/07/2014
03/08/2014
19/04/2015
13/06/2015
10/05/2016
23/07/2016
14/10/2016
06/05/2017
26/06/2017
28/06/2017
24/07/2017
10/08/2017
04/04/2018
11/06/2018
16/07/2018
21/07/2018
29/10/2018
01/11/2018
01/11/2018
22/04/2019
07/06/2019
08/06/2019
09/06/2019
10/06/2019
14/06/2019
15/06/2019
21/06/2019
22/06/2019
23/10/2019

1220

Table A1: Dates of the 29 anomalously electrified structures detected over the 2014-2019 period. The 8 events that occurred in June 2019 and are standing for 27.6 % of all 29 events are mentioned in bold.